Angular Distribution Models for Top-of-Atmosphere Radiative Flux Estimation from the Clouds and the Earth's Radiant Energy System Instrument on the Tropical Rainfall Measuring Mission Satellite.

Part I: Methodology

Norman G. Loeb[1]

*Center for Atmospheric Sciences, Hampton Universit*y, Hampton, Virginia

Natividad Manalo-Smith

Analytical Services and Materials, Hampton, Virginia

Seiji Kato

*Center for Atmospheric Sciences, Hampton Universit*y, Hampton, Virginia

Walter F. Miller

Science Applications International Corporation, Hampton, Virginia

Shashi K. Gupta

Analytical Services and Materials, Inc.

Patrick Minnis and Bruce A. Wielicki

NASA Langley Research Center, Hampton, Virginia

---

[1] *Corresponding Author Address*: Dr. Norman G. Loeb, Mail Stop 420, NASA Langley Research Center, Hampton, VA 23681-2199, U.S.A.

Abstract

Clouds and the Earth's Radiant Energy System (CERES) investigates the critical role that clouds and aerosols play in modulating the radiative energy flow within the Earth-atmosphere system. CERES builds upon the foundation laid by previous missions, such as the Earth Radiation Budget Experiment (ERBE), to provide highly accurate top-of-atmosphere (TOA) radiative fluxes together with coincident cloud and aerosol properties inferred from high-resolution imager measurements. This paper describes the methodology used to construct empirical Angular Distribution Models (ADMs) for estimating shortwave (SW), longwave (LW) and window (WN) top-of-atmosphere (TOA) radiative fluxes from CERES radiance measurements on board the Tropical Rainfall Measuring Mission (TRMM) satellite. To construct the ADMs, multi-angle CERES measurements are combined with coincident high-resolution Visible Infrared Scanner (VIRS) measurements and meteorological parameters from the European Centre for Medium-Range Weather Forecasts (ECMWF) data assimilation product. The ADMs are stratified by scene types defined by parameters that have a strong influence on the angular dependence of the Earth's radiation field at the TOA. Examples of how the new CERES ADMs depend upon the imager-based parameters are provided together with comparisons with existing models.

1. Introduction

The need for accurate global observations of top-of-atmosphere (TOA) radiative fluxes combined with coincident cloud and aerosol properties is critical for improved understanding and modeling of climate processes (Wielicki et al., 1995). Previous radiation budget experiments, such as the Earth Radiation Budget Experiment (ERBE) (Barkstrom, 1984) and the Scanner for Radiation Budget (ScaRaB) (Kandel et al., 1998), have generally provided accurate broadband radiative fluxes, but no cloud or aerosol properties. Conversely, experiments such as the International Satellite Cloud Climatology Project (ISCCP) (Rossow and Schiffer, 1991) and the Global Aerosol Climatology Project (Geogdzhayev et al., 2002) have provided the first global satellite cloud and aerosol climatologies, but no broadband TOA radiative fluxes. The central objective of the Clouds and the Earth's Radiant Energy System (CERES) mission is to provide accurate global cloud, aerosol and radiation data products to investigate the role that clouds and aerosols play in modulating the radiative energy flow within the Earth-atmosphere system. CERES will also provide the first global estimates of radiative fluxes at several atmospheric layers as well as the surface.

A critical component of CERES is the conversion of measured radiances to TOA fluxes. Since satellite radiometers can only instantaneously measure radiances in a limited number of viewing directions, while albedo or flux requires radiances from all angles, models of the bidirectional reflection and emission properties of the Earth at the TOA are needed. Previous investigations (e.g., ERBE) have developed empirical scene-dependent Angular Distribution Models (ADMs) to convert each measured radiance to a radiative flux estimate (Suttles et al., 1988, 1989). An alternate approach is to combine multi-angle radiance measurements from a

scene and use theoretical or empirical bidirectional reflectance models to infer TOA fluxes. Such a strategy is currently being used with narrowband multi-angle instruments such as POLDER (POLarization and Directionality of the Earth's Reflectances) (Buriez et al., 1997) and MISR (Multi-angle Imaging SpectroRadiometer) (Diner et al., 1999). While this approach may provide accurate instantaneous TOA fluxes (Diner et al., 1999; Chambers et al., 2001), errors in regional time-space averaged TOA fluxes tend to be larger than those based on a single-view TOA flux estimation technique applied to measurements from crosstrack scanning instruments (Stowe et al., 1994). This is because the spatial sampling of multi-angle measurements is less uniform than that of scanning crosstrack measurements, which is nearly contiguous over large areas.

The CERES strategy for radiance-to-flux retrievals is to use multi-angle broadband CERES measurements combined with coincident high spatial-resolution spectral imager measurements to construct empirical Angular Distribution Models (ADMs). The ADMs are determined for scene types defined by imager-derived parameters that have a strong influence on the anisotropy (or angular variation) of the radiance field. An instantaneous TOA flux estimate is determined for each measurement by applying the appropriate ADM corresponding to the measurement. The approach is similar to that used by ERBE (Suttles et al., 1988, 1989), but involves a far greater number of scene types ($\approx$200 SW and several hundred LW CERES ADM scene types, compared to 12 ERBE ADM scene types). By improving scene identification and increasing ADM model sensitivity to parameters that strongly influence anisotropy, CERES will improve TOA flux accuracy for individual cloud types, thereby providing a more reliable dataset for studying radiative processes and radiative forcing by cloud type.

This paper is the first in a three-part series. Here, a description of how the CERES shortwave (SW), longwave (LW) and window (WN) ADMs are derived for the CERES

instrument on board the Tropical Rainfall Measuring Mission (TRMM) satellite is provided. Because it is not feasible to provide detailed information on every CERES/TRMM ADM in this paper, a web page (at http://asd-www.larc.nasa.gov/Inversion/) has been created with figures and tabulations of the complete CERES/TRMM ADMs. Parts II and III will present extensive validation results in order to assess the accuracy of SW, LW and WN TOA fluxes derived from the CERES/TRMM ADMs. Because the TRMM orbit is restricted to 35°S-35°N, the CERES/TRMM ADMs are applicable only for tropical regions. A set of global ADMs are under development based on CERES and MODIS (Moderate Resolution Imaging Spectroradiometer) observations on Terra and, eventually, Aqua.

2. Observations

The CERES/TRMM instrument was launched on November 27, 1997, along with four other instruments. The TRMM spacecraft is in a 350-km circular, precessing orbit with a 35° inclination angle. TRMM has a 46-day repeat cycle, so that a full range of solar zenith angles is acquired over a region every 46 days. The CERES instrument is a scanning broadband radiometer that measures filtered radiances in the SW (wavelengths between 0.3-5 μm), total (TOT) (wavelengths between 0.3-200 μm) and window (WN) (wavelengths between 8-12 μm) regions. On TRMM, CERES has a spatial resolution of approximately 10 km (equivalent diameter) and operates in three scan modes: crosstrack, alongtrack, and rotating azimuth plane (RAP) mode. In RAP mode, the instrument scans in elevation as it rotates in azimuth, thus acquiring radiance measurements from a wide range of viewing configurations. CERES/TRMM scans in crosstrack mode for two consecutive days followed by RAP mode on the third day.

Starting in mid-April 1998, alongtrack scanning was invoked every 15 days and replaced the RAP scanning that would have occurred on the affected days.

Radiometric count conversion algorithms convert raw level-0 CERES digital counts into filtered radiances, using calibration (count conversion) coefficients that are derived from ground laboratory measurements (Priestley et al. 1999). The CERES instrument on TRMM was shown to provide an unprecedented level of calibration stability ($\approx$0.25%) between in-orbit and ground calibration (Priestley et al., 1999). To remove the influence of the instrument filter functions from the measurements, filtered radiances are converted to unfiltered reflected SW, emitted LW and emitted WN radiances using the approach described in Loeb et al. (2001). The unfiltered SW and LW radiances provide the reflected solar and emitted thermal radiation over the entire spectrum, respectively, in a given viewing direction. Unfiltered WN radiances correspond to emitted thermal radiation over the 8.1-11.8 μm wavelength interval only.

Unfortunately, the CERES instrument on board TRMM suffered a voltage converter anomaly in August 1998 and was turned off in September 1998 after 8 months of science data collection. CERES/TRMM was turned back on in March 2000 in order to acquire data that overlapped with measurements from the two CERES instruments on board the Terra spacecraft, launched on December 18, 1999. The CERES/TRMM instrument acquired only one more month of science data before the voltage converter anomaly caused irreparable damage to electronic components downstream of the converter. Consequently, only nine months of CERES/TRMM measurements are available for science use. Fortunately, improved voltage converters were installed prior to the launch of all CERES instruments on Terra and Aqua.

All nine months of the CERES/TRMM Single Scanner Footprint TOA/Surface Fluxes and Clouds (SSF) product from January-August 1998 and March 2000 between approximately

4

35°S and 35°N are used to develop CERES/TRMM ADMs. The CERES SSF product combines CERES radiances and fluxes with scene identification information inferred from coincident high spatial and spectral resolution Visible Infrared Scanner (VIRS) measurements. VIRS, which flew along with CERES on the TRMM spacecraft, consists of a five-channel imaging spectroradiometer that measures radiation at 0.63 μm, 1.61 μm, 3.78 μm, 10.8 μm and 12.0 μm at a spatial resolution of 2.11 km (Kummerow et al., 1998). VIRS scans in the crosstrack direction to a maximum viewing zenith angle of 48°. During the 9 months of CERES data acquisition, the SSF product was produced for 269 days. During this period, CERES was in crosstrack mode for 192 days, RAP mode for 68 days and alongtrack mode for 9 days.

The scene identification information derived from VIRS includes several aerosol and cloud parameters over each CERES footprint (**Section 3**). To optimize spatial matching between CERES measurements and imager-based cloud and aerosol properties, imager retrievals within CERES field-of-views (FOVs) are weighted by the CERES Point Spread Function (PSF) (Smith, 1994). Also included in the SSF product are meteorological fields for each CERES FOV based on European Centre for Medium-Range Weather Forecasts (ECMWF) data assimilation analysis (Rabier et al., 1998). A comprehensive description of all parameters appearing in the CERES SSF product is provided in the CERES Collection Guide (Geier et al., 2001).

Footprint location (geodetic latitude and longitude) and viewing geometry is defined using a reference level at the surface in the SSF product. Only CERES footprints that at least partially lie within the VIRS imager swath and whose centroids can be located on the Earth's surface are retained. As a result, when CERES is in crosstrack mode, only footprints with CERES viewing zenith angles ≤ 49° appear in the SSF product. Footprints with CERES viewing zenith angles > 49° are only present when CERES is either in RAP or alongtrack mode. Because

the SSF product is restricted to footprints whose centroids can be located on the Earth's surface, the maximum viewing zenith angle of a CERES footprint is 90°. Note that these restrictions are limited only to the CERES SSF product—all available CERES footprints are retained in the CERES ES-8 (ERBE-Like) product.

3. CERES ADM Scene Identification

One of the major advances in CERES/TRMM is the availability of coincident high spatial and spectral resolution VIRS measurements. Previous studies (e.g., Loeb et al., 2000; Manalo-Smith et al., 2001) have demonstrated that changes in the physical and optical properties of a scene have a strong influence on the anisotropy of the radiation at the TOA. Ignoring these effects results in large TOA flux errors (Chang et al., 2000). The following sections provide a brief overview of the CERES cloud mask, aerosol and cloud property retrieval algorithms, and the cloud layering and aerosol/cloud property convolution procedures used to provide scene identification for CERES footprints.

3.1 CERES Cloud Mask

To determine the cloud cover over a CERES footprint, the CERES cloud mask (Trepte et al., 1999; Minnis et al., 1999) is applied to all VIRS pixels that lie within a CERES footprint. The cloud mask consists of a series of threshold tests applied to all five VIRS spectral channels during the daytime ($\theta_o < 78°$, where θ_o is the solar zenith angle at the VIRS pixel), and three channels (3.78 μm, 10.8 μm and 12.0 μm) at night. If the observed radiances deviate significantly from expected clear-sky radiances in at least one of the available channels, a pixel is classified as cloudy. A cloudy pixel can be classified as either glint, "weak" cloud or "strong" cloud, depending on how much its radiances deviate from the predicted clear-sky radiances. A

6

clear pixel is classified as "weak", "strong", or "aerosol", where "aerosol" can be smoke, dust, ash, oceanic haze or "other" (e.g., when a combination of aerosols is detected or when algorithms cannot distinguish between two or more aerosol types). Expected clear-sky radiances are determined on a 10' latitude-longitude grid. Clear-sky albedo maps (Sun-Mack et al., 1999), directional reflectance models, and bi-directional reflectance functions are used to predict expected clear-sky radiances in the 0.63 μm, 1.6 μm and 3.75 μm channels (Minnis et al., 1999). Top-of-atmosphere brightness temperatures at 3.75 μm, 10.8 μm and 12 μm are determined using surface skin temperatures and atmospheric profiles from numerical weather analyses and empirical spectral surface emissivities (Chen et al., 1999). Surface elevation, vegetation type and up-to-date snow coverage maps are also used to determine the expected clear-sky radiances.

The daytime cloud mask involves a 3-step analysis of each pixel. The first step is a simple IR test that flags the pixels that are so cold they must be a cloud. Over ocean, this condition occurs if the VIRS 10.8 μm channel brightness temperature is more than 20°C below the ocean surface skin temperature. For most land surfaces a pixel is flagged as cloudy if its 10.8 μm channel brightness temperature is smaller than the temperature at 500 hPa. A temperature corresponding to a lower pressure is used for surface pressures less than 600 hPa. The second step involves a series of three tests comparing the pixel to a known background or clear-sky value for 0.63 μm reflectance, 10.8 μm brightness temperature and 3.75-10.8 μm brightness temperature difference. If all three tests unanimously determine the pixel to be clear (cloudy), this pixel is labeled "strong" clear (cloudy). If one or two tests fail, a series of additional tests involving the ratio of 1.6 μm to 0.63 μm reflectances and/or the difference between 11 μm and 12 μm brightness temperatures are applied in order to determine whether a pixel is "weak" or "strong" clear/cloud.

The first step in the nighttime cloud mask is identical to the initial daytime brightness temperature test. The next step consists of tests comparing a pixel's brightness temperature and brightness temperature difference (3.75 µm - 11 µm) to pre-determined clear-sky values. If either test fails to identify the pixel as clear, then a set of additional tests with a different set of thresholds is used to determine whether a pixel is "weak" clear or "weak/strong" cloud (see Trepte et al., 1999).

Over very hot land and desert, the VIRS thermal channels may saturate. To avoid misclassifying clear CERES footprints due to saturated VIRS data, the CERES WN filtered radiance is tested for the possibility that the scene may be clear. This test is used when the VIRS thermal radiance in a CERES footprint is flagged "bad" and the VIRS 0.63 µm channel contains a good radiance. If the CERES WN filtered radiance exceeds a predetermined threshold, the footprint is reclassified as "clear" and a flux is determined from CERES. Otherwise, the scene type is assumed "unknown". The predetermined CERES WN filtered radiance is derived from radiative transfer model simulations in 5° viewing zenith angle increments over a hot desert scene with a dry tropical atmosphere and a surface temperature of 314 K (Kratz, 2001, private communication). Between 35°S and 35°N, saturation occurs in less than 0.5% of the observations. Most of these occurrences are for daytime scenes over desert during the summer months.

3.2 Aerosol and Cloud Property Retrieval Algorithm

Aerosol optical depths from VIRS pixels identified as clear are inferred from 0.63 µm VIRS radiances based on the retrieval algorithm of Ignatov and Stowe (2002). The algorithm uses a single-channel look-up table approach based on radiances computed from the 6S radiative transfer model (Vermote et al, 1997). Aerosols are assumed to be nonabsorbing and are

8

represented by a lognormal particle size distribution with a modal radius of 0.1 μm and a standard deviation in the logarithm of particle radius of 2.03 μm. These particle size distribution parameters were determined by fitting Mie calculations for a mono-modal lognormal size distribution to an empirically derived phase function (Ignatov, 1997).

Radiances from VIRS pixels identified as cloudy are analyzed to estimate parameters that characterize the optical and physical properties of the cloud. These parameters include cloud visible optical depth, infrared emissivity, phase, liquid or ice water path, cloud top pressure and particle effective size. The algorithm consists of an iterative inversion scheme to determine the cloud properties which, when input into a plane-parallel radiative transfer model, yield the best match to observed radiances at a particular satellite viewing geometry. A detailed description of the retrieval algorithm and initial results is provided in Minnis et al. (1995), Minnis et al. (1998), and Minnis et al. (1999). Cloud top height and pressure are determined from the retrieved cloud top temperature using the nearest vertical temperature and pressure profiles from numerical weather analyses. Liquid and ice water paths are derived from retrievals of cloud optical depth and particle effective size.

In cases where the cloud algorithm cannot determine a solution for the observed radiances, a second cloud mask based on Welch et al. (1992) is used to reassess whether the pixel is really cloudy. The pixel is reclassified as clear if this second cloud mask determines it to be clear. Otherwise, the pixel is labeled as "cloudy no retrieval". The no retrieval classification is used for approximately 4% of all cloudy cases.

3.3 CERES Point Spread Function Convolution and Cloud Layering

Accurate relationships between aerosol, cloud and radiative fluxes require accurate spatial and temporal matching of imager-derived aerosol and cloud properties with CERES broadband

radiation data. When CERES is in crosstrack mode, VIRS and CERES observe a scene simultaneously. However, scenes observed by CERES in the alongtrack direction at oblique viewing zenith angles are observed by VIRS within $\approx$2 minutes of CERES. To achieve the closest spatial match between CERES and VIRS, the distribution of energy received at the CERES broadband detectors must be taken into account when averaging imager-derived properties over the CERES footprint. This distribution of energy is described by the CERES point spread function (Smith, 1994). The point spread function accounts for the effects of detector response, optical field of view and electronic filters. To determine appropriately weighted and matched aerosol and cloud properties within CERES fields of view, pixel-level imager-derived aerosol and cloud properties are convolved with the CERES point spread function.

Within a CERES footprint, the properties of every cloudy imager pixel are assigned to a cloud layer. If there is a significant difference in cloud phase or effective pressure within a CERES FOV, up to two non-overlapping cloud layers are defined. In general, a single footprint may contain any combination of clear area and one or two distinct cloud areas (**Figure 1**).

To determine whether two distinct cloud layers are present, the imager pixels are initially binned by phase into either water or ice categories. Two distinct cloud layers are present if (i) the mean and standard deviation of effective cloud pressure from the two populations are significantly different based on a Student t test (at the 95% confidence interval) and (ii) the mean cloud effective pressure differs by more than 50 hPa. If both conditions are met, a threshold effective pressure is defined at the mid-point between the effective pressures of the lowest and highest cloud layers. The imager pixels are then re-categorized using the threshold effective pressure before the point spread function weighted average cloud properties are determined for each layer.

If this method fails to identify two distinct cloud layers, a second approach is considered. The pixel-level cloud effective pressures are sorted from lowest to highest. The largest gap in this series (exceeding 50 hPa) is used to separate pixels into two cloud layers. The Student t test is then performed on the mean and standard deviation of the cloud effective pressures for these two populations. If they are statistically different, they are convolved over the footprint as two separate layers. If the pixels fail to meet these minimum requirements, they are assigned to one layer. When present, multilayer imager pixels (e.g., thin cirrus over low cloud) are identified with an overlapped cloud detection algorithm (Baum et al., 1999), but cloud properties are retrieved and convolved as if only one layer were present. The overlapped cloud detection algorithm only identifies multilayer clouds when a well-defined thin upper-level cloud layer lies above a well-defined lower-level cloud (Baum et al., 1999).

3.4   Cloud Effective Parameters over CERES Footprints

The cloud fraction over a CERES footprint is determined from: $1 - A_{clr}$, where A_{clr} is the imager clear area fractional coverage. A cloud fraction is determined only over the part of a CERES footprint that has imager coverage. Footprints near the edge of the VIRS swath have only partial coverage by VIRS. Partial imager coverage can also be due to bad imager data or because a pixel cannot be determined clear or cloudy by the CERES cloud mask. All full and partial Earth-view CERES FOVs containing at least one imager pixel are recorded in the SSF product. The effective mean of a parameter x over a CERES footprint is derived from the PSF-weighted layer mean values as follows:

$$\overline{x} = \frac{A_1 x_1 + A_2 x_2}{A_1 + A_2} \tag{1}$$

where A_1 and A_2 are the fractional coverage of layers 1 and 2, respectively, over a CERES

footprint.

Under some conditions a pixel can be identified as cloudy, but the cloud algorithm may fail to determine cloud properties from the observed radiances. These cases, referred to as "no retrievals", can occur alongside pixels where the cloud algorithm does provide cloud properties. When this occurs, the region where retrievals are available is assumed to provide the mean cloud properties over the CERES footprint. That is, we assume that the cloud mean properties over the region of "no retrievals" are the same as over the region where retrievals are available.

Since CERES relies on the imager to identify the scene within a footprint, a minimum amount of imager coverage and cloud property information is needed in order to construct ADMs. The total fraction of unknown cloud properties over the footprint is determined by combining the imager coverage (A_{im}) and the fraction of the cloudy area lacking cloud properties (A_{ncl}) as follows:

$$A_{unk} = (1 - A_{im}) + A_{im}(1 - A_{clr})A_{ncl} \qquad (2)$$

where the first term provides the fraction of the footprint with no imager coverage, and the second is the fraction of the footprint from the cloudy area with unknown cloud properties. In general, only footprints with $A_{unk} \leq 0.35$ are used to construct CERES ADMs. For cloudy scenes over ocean observed at glint angles (γ) less than 40°, only footprints with $A_{im} \geq 0.5$ are considered. γ is the angle between the reflected ray and the specular ray for a flat ocean given by:

$$\cos\gamma = \mu\mu_o + \sqrt{(1-\mu)^2}\sqrt{(1-\mu_o)^2}\cos\phi \qquad (3)$$

where μ and μ_o are the cosine of the viewing and solar zenith angles, respectively, and ϕ is the relative azimuth angle. Over all surfaces except snow, cloudy footprints must have a valid cloud optical depth in the lower layer to be considered. While footprints with insufficient imager

coverage or cloud property information are not considered when constructing the ADMs, a flux estimate is nonetheless provided for these footprints when the ADMs are applied to determine TOA fluxes. The strategy for estimating fluxes from footprints with insufficient imager or cloud property information is described in **Section 5.3**.

4. CERES ADM Development

TOA flux is the radiant energy emitted or scattered by the Earth-atmosphere per unit area. Flux is related to radiance (I) as follows:

$$F(\theta_o) = \int_0^{2\pi} \int_0^{\pi/2} I(\theta_o, \theta, \phi) \cos\theta \, \sin\theta \, d\theta d\phi \tag{4}$$

where θ_o is the solar zenith angle, θ is the observer viewing zenith angle, and ϕ is the relative azimuth angle defining the azimuth angle position of the observer relative to the solar plane (**Figure 2**). An ADM is a function (R) that provides anisotropic factors for determining the TOA flux from an observed radiance as follows:

$$F(\theta_o) = \frac{\pi I(\theta_o, \theta, \phi)}{R(\theta_o, \theta, \phi)} \tag{5}$$

Since CERES measures the upwelling radiation from a scene at any given time from one or more directions, F (or R) cannot be measured instantaneously. Instead, R is obtained from a set of pre-determined empirical ADMs defined for several scene types with distinct anisotropic characteristics. Each ADM is constructed from a large ensemble of radiance measurements that are sorted into discrete angular bins and parameters that define an ADM scene type. The ADM anisotropic factors for a given scene type (j) are given by:

$$R_j(\theta_{oi}, \theta_k, \phi_l) = \frac{\pi \overline{I}_j(\theta_{oi}, \theta_k, \phi_l)}{F_j(\theta_{oi})} \tag{6}$$

where $\bar{I}_j$ is the average radiance (corrected for Earth-sun distance in the SW) in angular bin $(\theta_{oi}, \theta_k, \phi_l)$, and F_j is the upwelling flux in solar zenith angle bin θ_{oi}. The set of angles $(\theta_{oi}, \theta_k, \phi_l)$ corresponds to the midpoint of a discrete angular bin defined by $(\theta_{oi} \pm \frac{\Delta\theta_o}{2}$, $\theta_k \pm \frac{\Delta\theta}{2}$, $\phi_l \pm \frac{\Delta\phi}{2})$, where $\Delta\theta_o$, $\Delta\theta$ and $\Delta\phi$ represent the angular bin resolution (**Figure 3**). Relative azimuth angles range from 0° to 180° because the models are assumed to be azimuthally symmetric about the principle plane. Angular bins for θ_o are defined over the same intervals as for θ. In the SW R_j is a function of all three angles, while in the LW and WN regions R_j is defined as a function of viewing zenith angle only. While the dependence of LW and WN anisotropy on solar zenith angle and relative azimuth angle is negligible in most conditions, Minnis and Khaiyer (2000) showed that for clear land regions, especially those consisting of rough terrain, LW anisotropy depends systematically on relative azimuth angle. This occurs because warm, solar illuminated surfaces are observed in the backscattering direction, whereas cooler, shadowed surfaces are observed in the forward scattering direction. Thus, in certain viewing configurations errors in LW TOA fluxes of up to 7 W m^{-2} can occur in clear mountainous regions (David Doelling, 2002, private communication). Similar azimuthal dependencies may also occur in broken or thin-cloud conditions.

To determine $\bar{I}_j$ in Eq. (6), instantaneous radiances for each scene type are first averaged daily in angular bins half the size of the CERES/TRMM ADM angular bins. In the SW, this means that up to 8 sub-resolution angular bin average radiances (2 solar zenith angle bins× 2 viewing zenith angle bins × 2 relative azimuth angle bins) can be used to determine $\bar{I}_j$ for every CERES angular bin. In the LW and WN regions, two sub-resolution angular bins are available since the LW and WN ADMs are a function of viewing zenith angle only. A CERES angular bin

is assumed to have sufficient sampling in the SW only if at least 5 of the 8 sub-resolution angular bins have been observed by CERES. In the LW and WN regions, both sub-resolution viewing zenith angle bins must have measurements. An ADM is defined only when at least 75% of the viewing zenith angle and relative azimuth angle bins for a given solar zenith angle bin have sufficient sampling. A total of 269 CERES/TRMM days are used to determine SW mean radiances, while only 77 RAP and alongtrack days are used to determine mean LW and WN radiances.

For CERES/TRMM, the Earth's surface covers the entire instrument FOV (i.e., "full-Earth" view) for θ between 0° and 80° when θ is defined at the surface reference level. In this range, radiances are generally available in the SSF product. However, because at least part of a CERES footprint must lie within the VIRS imager swath to be included in the SSF, the number of footprints from oblique CERES viewing zenith angles is limited. For θ between 80° and 90°, the footprint centroid intersects the Earth, but the leading edge of the footprint in the along-scan direction lies beyond the Earth tangent point (i.e., "partial-Earth" view). Since imager pixels are unavailable beyond the Earth's tangent point, only the part of the CERES FOV covered by the Earth has imager coverage. Consequently, scene identification for CERES footprints with viewing zenith angles > 80° is unreliable, and these footprints are not used to determine scene-type dependent ADMs.

To calculate the upwelling flux for a given scene type, average radiances in all angular bins are needed. Unfortunately, this is not always feasible from satellite measurements. Average radiances for angular bins with missing data are estimated by using either directional reciprocity or radiative transfer theory. Directional reciprocity is used only for SW ADM types that are cloud-free (Di Girolomo et al., 1998). The procedure for filling in angular bins using directional

reciprocity is described in Suttles et al. (1988). For missing angular bins where directional reciprocity is not used, the average radiance is estimated from a combination of observed radiances in angular bins where data are available and theoretical radiances as follows:

$$\hat{\bar{I}}_j(\theta_{oi},\theta_p,\phi_q) = \frac{1}{mn}\sum_{k=1}^{m}\sum_{l=1}^{n}\bar{I}_j(\theta_{oi},\theta_k,\phi_l)\left(\frac{I^{th}(\theta_{oi},\theta_p,\phi_q)}{I^{th}(\theta_{oi},\theta_k,\phi_l)}\right) \tag{7}$$

where $\hat{\bar{I}}_j(\theta_{oi},\theta_p,\phi_q)$ corresponds to the estimated radiance for an angular bin, $\bar{I}_j(\theta_{oi},\theta_k,\phi_l)$ corresponds to an observed mean radiance, and I^{th} is a theoretically derived radiance. The summation limits, m and n, correspond to the number of angular bins where $\bar{I}_j(\theta_{oi},\theta_k,\phi_l)$ is available. The theoretical radiances are selected from a database of plane-parallel, horizontally homogeneous radiative transfer simulations for Earth scenes under a wide range of conditions. For a given surface type and cloud category (e.g., clear ocean, cloud over land, etc.), the specific theoretical radiances in Eq. (7) are determined from the model simulation that minimizes the root-mean-square difference in radiance between theory and observations in the angular bins where data are available. In the SW, the radiative transfer calculations are based on the DISORT radiative transfer code (Stamnes et al., 1988), while in the LW, radiances are based on a code by Gupta et al. (1985). The **Appendix** describes the cases that comprise the theoretical radiance database.

To determine F_j, the usual approach is to explicitly integrate $\bar{I}_j$ using a discrete form of Eq. (4). However, as pointed out by Loeb et al. (2002), radiance contributions from the entire Earth disk and overlying atmosphere must be taken into account, including radiances that emerge from the atmosphere along slant atmospheric paths beyond the Earth's horizon (i.e. above the Earth's tangent point). Ignoring these radiance contributions can cause a 1-2 W m^{-2} underestimation in TOA flux. To account for these contributions, Loeb et al. (2002) showed that

the FOV reference level must be defined at least at 100 km above the Earth's surface. To convert the viewing zenith angle from a surface FOV reference level to a 100-km FOV reference level, the following transformation is used:

$$\sin\theta(h_{100}) = \left(\frac{r_e + h_{sfc}}{r_e + h_{100}}\right)\sin\theta(h_{sfc}) \tag{8}$$

where $\theta(h_{sfc})$ is the viewing zenith angle at the surface reference level, and r_e is the mean radius of the Earth (which is set to 6371 km).

At a 100-km FOV reference level, the CERES centroid intersects the Earth's surface for angles $\theta(h_{100})$ between 0° and 79.9° (region I in **Figure 4**), where $\theta(h_{100})$ denotes viewing zenith angles defined at the 100-km FOV reference level. For this range of angles, $\bar{I}_j$ is determined from the measurements, as described above. For $\theta(h_{100}) > 79.9°$, the CERES footprint centroid lies beyond the Earth tangent point, and the number of CERES footprints in the SSF at these angles is limited due to the narrow VIRS swath. For clear scenes, as $\theta(h_{100})$ increases beyond 79.9°, the radiance decreases rapidly, and eventually approaches zero as CERES begins to observe cold space. To estimate radiances for $\theta(h_{100}) > 79.9°$, MODTRAN (Kneizys et al., 1996) simulations for a molecular atmosphere are used. If the scene type is cloudy, however, the MODTRAN molecular atmosphere approximation is only used at observer viewing zenith angles where the FOV centroid lies above the cloud top (region III in **Figure 4**). The cloud top height is given by the average effective cloud top height of all footprints in the ADM class. For most clouds, the observer viewing zenith angle corresponding to the cloud top is close to that for the Earth tangent point (i.e., $\theta(h_{100})=79.9°$). For example, for a cloud at 5 km $\theta(h_{100})=80.17°$, while for a cloud at 15 km $\theta(h_{100})=80.7°$. In the narrow range of angles

17

between the Earth tangent point and cloud top (region II in **Figure 4**), radiances are extrapolated from radiances at $\theta(h_{100}) < 79.9°$.

The reflected shortwave and emitted longwave ADM fluxes are determined as follows:

$$F_j^{SW}(\theta_{oi}; h_{100}) = \sum_{l=1}^{N_l} w_l \left\{ \sum_{k=1}^{N_k} w_k \overline{I}_j^{SW}(\theta_{oi}, \theta_k, \phi_l; h_{100}) \cos\theta_k \right\} \tag{9}$$

$$F_j^{LW}(h_{100}) = \sum_{k=1}^{N_k} w_k \overline{I}_j^{LW}(\theta_k; h_{100}) \cos\theta_k \tag{10}$$

where w_k and w_l are Gaussian quadrature weights for integration over viewing zenith angles from 0° to 90°, and relative azimuth angles from 0° to 180°, respectively. The number of Gaussian quadrature points (i.e., N_k and N_l) used to evaluate Eqs. (9) and (10) is 200. Radiances at the Gaussian points are determined by linearly interpolating the mean radiances defined over the CERES angular bins.

Since the viewing geometry and footprint geolocation in the SSF product are provided at the surface reference level, the CERES ADMs are defined so that they also correspond to the surface reference level. The SW and LW ADMs at the surface reference level are given by:

$$R_j^{SW}(\theta_{oi}, \theta_k, \phi_l; h_{sfc}) = \frac{\pi \overline{I}_j^{SW}(\theta_{oi}, \theta_k, \phi_l; h_{sfc})}{F_j^{SW}(\theta_{oi}; h_{100})} \left(\frac{r_e}{r_e + h_{100}} \right)^2 \tag{11}$$

$$R_j^{LW}(\theta_k; h_{sfc}) = \frac{\pi \overline{I}_j^{LW}(\theta_k; h_{sfc})}{F_j^{LW}(h_{100})} \left(\frac{r_e}{r_e + h_{100}} \right)^2 \tag{12}$$

Since $\overline{I}_j$ in Eq. (6) is inferred from daily mean radiances, an estimate of the variability in the SW ADMs can be inferred from the standard deviation in daily mean radiances as follows:

$$\varepsilon_{R_j}(\theta_{oi}, \theta_k, \theta_l) = t_{p,n} \frac{\pi}{F_j(\theta_{oi})} \left(\frac{\sigma_{\overline{I}_j}(\theta_{oi}, \theta_k, \theta_l)}{\sqrt{N_{\overline{I}_j}(\theta_{oi}, \theta_k, \theta_l)}} \right) \tag{13}$$

18

where $t_{p,n}$ is the $100(1\text{-}p)^{\text{th}}$ percentile of the Student-t distribution with n degrees of freedom, and $\sigma_{\bar{I}_j}$ and $N_{\bar{I}_j}$ are the standard deviation and number of daily mean radiances in an angular bin, respectively. For the 95% confidence interval, $p=0.025$ and $n=(N_{\bar{I}_j}-1)$. A similar expression can also be used to estimate the variability in LW ADMs. Note that Eq. (13) is only an estimate of the ADM variability—the actual ADM variability would require knowledge of the standard deviation in daily mean anisotropic factors rather than the mean radiances.

5. Instantaneous TOA Flux Estimation

5.1 Interpolation Bias Correction

To estimate a flux from a radiance measurement the appropriate ADM scene type must first be determined from the imager retrievals. Next, Eq. (5) is applied using an estimate of the anisotropic factor. However, since the anisotropy of Earth scenes generally varies with viewing geometry and cloud/clear-sky properties in a continuous manner, whereas the CERES ADMs (Eqs. (11) and (12)) are defined for discrete angular bins and scene types, an adjustment to the CERES anisotropic factors is needed in order to avoid introducing large instantaneous flux errors or sharp flux discontinuities between angular bins or scene types. One way of reducing angular bin discretization errors is to obtain anisotropic factors by linearly interpolating bin-average ADM radiances (e.g., $\bar{I}_j^{SW}(\theta_{oi},\theta_k,\phi_l;h_{sfc})$) and fluxes (e.g., $F_j^{SW}(\theta_{oi};h_{sfc})$) to each observation angle (θ_o,θ,ϕ), and evaluating anisotropic factors from Eq. (6) using the interpolated quantities. In addition, interpolation over other parameters that influence anisotropy (e.g., cloud optical depth) can also be used. In some cases it may even be advantageous to combine empirical and

theoretical ADMs to estimate the anisotropic factor at a particular angle (e.g., clear ocean SW ADMs in **Section 6.1**).

When linear interpolation is used, the instantaneous TOA flux is given by:

$$\hat{F}(\theta_o,\theta,\phi;h_{sfc}) = \frac{\pi I(\theta_o,\theta,\phi;h_{sfc})}{\tilde{R}_j(\theta_o,\theta,\phi;h_{sfc})} \tag{14}$$

where $\tilde{R}_j(\theta_o,\theta,\phi;h_{sfc})$ represents an anisotropic factor at the surface reference level determined from interpolated ADM radiances ($\tilde{I}_j(\theta_o,\theta,\phi;h_{sfc})$) and fluxes ($\tilde{F}_j(\theta_o;h_{sfc})$). While instantaneous flux errors are likely reduced with this approach, there is no guarantee that ensemble averages of the instantaneous fluxes will remain unbiased. A bias in the mean flux will occur if linear interpolation is used when the actual radiance varies nonlinearly within an angular bin. It also occurs when theoretical models are used to supplement empirical ADMs. The bias for a specific scene type j in angular bin ($\theta_{oi},\theta_k,\phi_l$) is determined from the difference between the estimated mean flux and the ADM mean flux (determined by direct integration of radiances) as follows :

$$\Delta F_j(\theta_{oi},\theta_k,\phi_l;h_{sfc}) = \left\langle \frac{\pi I(\theta_o,\theta,\phi;h_{sfc})}{\tilde{R}_j(\theta_o,\theta,\phi;h_{sfc})} \right\rangle_{ikl} - F_j(\theta_{oi};h_{sfc}) \tag{15}$$

where the first term on the right-hand-side is the average of all instantaneous flux estimates from Eq. (14) falling in angular bin ($\theta_{oi} \pm \frac{\Delta\theta_o}{2}, \theta_k \pm \frac{\Delta\theta_k}{2}, \phi_l \pm \frac{\Delta\phi_l}{2}$) for scene type j, and $F_j(\theta_{oi};h_{sfc})$ is the corresponding ADM flux. To remove the bias, a correction term is added to instantaneous TOA fluxes:

$$\hat{F}'(\theta_o,\theta,\phi;h_{sfc}) = \frac{\pi I(\theta_o,\theta,\phi;h_{sfc})}{\tilde{R}_j(\theta_o,\theta,\phi;h_{sfc})} + \delta F_j(\theta_o,\theta,\phi;h_{sfc}) \tag{16}$$

where

$$\delta F_j(\theta_o,\theta,\phi;h_{sfc}) = -\frac{I(\theta_o,\theta,\phi;h_{sfc})}{\tilde{I}_j(\theta_o,\theta,\phi;h_{sfc})} \frac{\Delta F_j(\theta_{oi},\theta_k,\phi_l;h_{sfc})}{\left\langle \dfrac{I(\theta_o,\theta,\phi;h_{sfc})}{\tilde{I}_j(\theta_o,\theta,\phi;h_{sfc})} \right\rangle_{ikl}}$$
(17)

When the ensemble average of instantaneous TOA fluxes from Eq. (16) is determined, the mean flux is unbiased since $\overline{\delta F_j}(\theta_{oi},\theta_k,\phi_l;h_{sfc}) = \Delta F_j(\theta_{oi},\theta_k,\phi_l;h_{sfc})$. This procedure is used in all SW TOA flux estimates (except over snow). In the LW and WN channels, $\delta F_j(\theta)$ is close zero and is therefore not explicitly accounted for.

5.2   TOA Flux Reference Level

Based on theoretical radiative transfer calculations using a model that accounts for spherical Earth geometry, Loeb et al. (2002) recently showed that the optimal reference level for defining TOA fluxes in Earth radiation budget studies is approximately 20 km. This reference level corresponds to the effective radiative "top-of-atmosphere" since the radiation budget equation is equivalent to that for a solid body of a fixed diameter that only reflects and absorbs radiation. The TOA flux at the 20-km reference level (h_{20}) is determined from the flux at the surface reference level as follows:

$$\hat{F}'(\theta_o,\theta,\phi;h_{20}) = \hat{F}'(\theta_o,\theta,\phi;h_{sfc})\left(\frac{r_e}{r_e+h_{20}}\right)^2$$
(18)

On the CERES SSF product, instantaneous TOA fluxes are provided only for CERES radiances with $\theta(h_{sfc}) \leq 70°$ and $\theta_o \leq 86.5°$.

5.3 Footprints with Insufficient Imager Information

As noted in **Section 3.4**, CERES footprints sometimes lack sufficient imager information to define an ADM scene type because part of the footprint may lie outside the VIRS imager swath, the imager data are flagged as bad, or because the cloud algorithm fails to determine cloud properties from the observed radiances ("no retrievals"). If the total fraction of unknown cloud properties (defined in Eq. (2)) exceeds a threshold, the footprint is not used in ADM development. While it is tempting to also reject such footprints when applying the ADMs in determining instantaneous TOA fluxes, this could introduce systematic biases in the mean TOA flux if the "no retrievals" are correlated with cloud type (e.g., thin ice clouds). To avoid introducing potential biases in regional TOA flux estimates caused by systematic rejection of clouds whose optical properties fall outside the expected range of the retrieval model (resulting in "no retrievals"), instantaneous TOA fluxes are estimated regardless of what the total fraction of unknown cloud properties is over the footprint. While TOA flux estimates for these footprints likely have greater instantaneous errors than those derived with complete imager information, biases in the overall means will be avoided if the errors are random.

To determine a TOA flux for a footprint that lacks sufficient imager information to define an ADM scene type, ADM radiances (e.g., $\bar{I}_j^{SW}(\theta_{oi}, \theta_k, \phi_l; h_{sfc})$) are interpolated to the FOV viewing geometry and compared with the measured radiance. The anisotropic factor used to convert the measured radiance to flux is evaluated from the ADM whose interpolated radiance most closely matches the measured radiance. To constrain the result, only ADMs having the same underlying surface type as the measurement are considered as possible candidates. From the 9-month CERES/TRMM dataset, footprints with insufficient imager coverage to determine an ADM scene type occurs $\approx 7\%$ of the time.

5.4   Mixed-Scenes

When a CERES footprint contains a mixture of surface types (e.g., ocean and land, land and desert), instantaneous TOA fluxes are determined using the ADM that corresponds to the surface type with the highest percent coverage over the footprint. For example, near coastlines, if most of the footprint PSF-weighted area is over ocean, an ocean ADM is used to convert the radiance to flux. Conversely, if most of the footprint area is over land, one of the Land ADMs is used. An exception occurs when SW TOA fluxes are estimated from mixed land-ocean footprints in the sunglint region. In that case, if the glint angle (Eq. (3)) is $\leq 40°$ and the footprint is covered by more than 5% ocean, the footprint bidirectional reflectance is assumed to be closer to that for ocean, and one of the Ocean ADMs is used.

6.   SW ADM Scene Types

6.1   Clear Ocean

Clear footprints are defined as footprints with $\geq 99.9\%$ of VIRS imager pixels identified as cloud-free. Separate clear ocean ADMs are defined for four intervals of wind speed corresponding to the 0-25th, 25th-50th, 50th-75th and 75th-100th percentiles of the wind speed probability density distribution. These correspond to wind speed intervals of approximately < 3.5 m s^{-1}, 3.5-5.5 m s^{-1}, 5.5-7.5 m s^{-1} and > 7.5 m s^{-1}. The wind speeds, which correspond to the 10-m level, are based on Special Sensor Microwave/Imager (SSM/I) retrievals (Goodberlet et al., 1990) that have been ingested into the ECMWF data assimilation analysis. For a given wind speed interval, w_j, the ADM is defined following the procedure outlined in **Section 4**.

Since the anisotropy of clear ocean scenes also depends on aerosol optical depth, this dependence should also be accounted for when estimating SW fluxes over clear ocean. The SSF product provides aerosol optical depth retrievals (Ignatov and Stowe, 2000), but only in viewing conditions where the glint angle exceeds 40°. Consequently, it is not possible to construct empirical ADMs stratified by the Ignatov and Stowe (2000) aerosol optical depth retrievals since no information on how CERES radiances vary with aerosol optical depth in the glint region are available. As an alternative, instantaneous TOA fluxes are first inferred in any viewing geometry from wind speed dependent empirical ADMs. Next, these TOA flux estimates are adjusted as follows:

$$\hat{F}'(\theta_o,\theta,\phi;h_{sfc}) = \frac{\pi I(\theta_o,\theta,\phi;h_{sfc})}{\tilde{R}(w_j;\theta_o,\theta,\phi;h_{sfc})\left(\dfrac{R^{th}(w_j,I)}{R^{th}(w_j,\tilde{I})}\right)} + \delta F(w_j;\theta_o,\theta,\phi;h_{sfc}) \qquad (19)$$

where $\tilde{R}(w_j,\theta_o,\theta,\phi;h_{sfc})$ is determined from the wind speed dependent ADMs, and $R^{th}(w_j,I)$ and $R^{th}(w_j,\tilde{I})$ are anisotropic factors inferred from the measured CERES radiance $I(\theta_o,\theta,\phi;h_{sfc})$ and the interpolated ADM radiance ($\tilde{I}(\theta_o,\theta,\phi;h_{sfc})$), respectively. To determine $R^{th}(w_j,I)$ and $R^{th}(w_j,\tilde{I})$, CERES radiances $I(\theta_o,\theta,\phi;h_{sfc})$ and $\tilde{I}(\theta_o,\theta,\phi;h_{sfc})$ are compared with look-up tables of theoretical SW radiances stratified by aerosol optical depth. $R^{th}(w_j,I)$ and $R^{th}(w_j,\tilde{I})$ correspond to the aerosol optical depth for which the theoretical radiances match the CERES radiances. The radiative transfer calculations are based on the DISORT radiative transfer model (Stamnes et al., 1988) and assume maritime Tropical aerosols based on Hess et al. (1998) evaluated at 24 optical depths. The ocean surface in the calculations accounts for the bidirectional reflectance of the ocean at the five wind speeds corresponding to the midpoints of the CERES ADM wind speed intervals using the "OCEABRDF" subroutine from the 6S

radiative transfer code (Vermote et al., 1997). This routine accounts for specular reflection (Cox and Munk, 1954), wind-speed dependent whitecaps (Koepke, 1984), and below water surface reflectance (Morel, 1988).

Eq. (19) can be used to estimate TOA flux in any viewing geometry. However, as the satellite viewing geometry moves towards the ocean specular reflection direction, the radiance increase for a change in angle as small as 1° can be quite large. Because such changes are unresolved by the relatively coarse angular bins used to define CERES ADMs, instantaneous TOA flux estimates are generally unreliable for footprints near the specular reflection direction. Consequently, the radiance-to-flux conversion is not performed in these regions. However, ignoring these samples (e.g., by not providing a TOA flux estimate) can introduce biases in regional mean fluxes since fluxes over cloudy portions of a region will contribute disproportionately to the overall regional mean. To avoid this, fluxes in cloud-free sunglint are given by the clear ocean wind speed dependent ADM flux (F_j^{SW}) interpolated at the solar zenith angle of the observation.

To determine whether or not a footprint is too close to the specular reflection direction to provide a reliable flux retrieval, the derivatives of clear ocean ADM anisotropic factors with respect to illumination and viewing geometries ($\partial R_j / \partial \theta_o$, $\partial R_j / \partial \theta$, and $\partial R_j / \partial \phi$) are evaluated in each CERES angular bin. If an observation falls in an angular bin where one of the derivatives exceeds a threshold value, a radiance-to-flux conversion is not performed. In this study, a threshold of 0.075 per degree is used as the cutoff, which corresponds approximately to a 40° glint angle threshold.

6.2   Clear Land and Desert

The anisotropy of surface-leaving radiances over land and desert regions depends on several factors, including vegetation coverage, surface type and surface heterogeneity (Roujean et al., 1992). The intervening atmosphere modifies the surface anisotropy, particularly at shorter wavelengths (Zhou et al., 2001), and for large aerosol optical depth (Li et al., 2000). The observed anisotropy of TOA-leaving radiances also depends on instrument resolution since clear land scenes become more inhomogeneous when observed at larger spatial scales.

The inclined orbit of the TRMM satellite provides a unique opportunity for determining ADMs under all solar zenith angle conditions. To account for climatological differences between surface types, ADMs are first constructed for each of the International Geosphere Biosphere Programme (IGBP) Global Land Cover types (Belward and Loveland, 1996) for which there are sufficient data in the Tropics. CERES uses a 10' latitude by 10' longitude resolution map of IGBP types that covers the globe (Rutan and Charlock, 2001, private communication). The IGBP classification scheme is provided in **Table 1**, along with the fraction of cloud-free CERES footprints for each IGBP surface type category over the entire 9 months of daytime CERES/TRMM observations (last column). Over land and desert, Barren Desert (16) and Open Shrubs (7) account for 53% of the clear footprints, IGBP types with low-to-moderate tree/shrub coverage (i.e., IGBP types 9-14) account for 34%, and IGBP types with moderate-to-high tree/shrub coverage (i.e., IGBP types 1-6, 8) account for 13%. Unfortunately, there aren't enough data over the Tropics to construct ADMs for Deciduous Needleleaf Forests (3), Permanent Wetlands (11), and Urban (13) IGBP types.

Figure 5-Figure 6 show clear-sky ADM anisotropic factors for $\theta_o = 30°$-$40°$ for individual IGBP types (colored lines) together with ADMs determined by grouping all IGBP

types falling in the moderate-to-high and low-to-moderate tree/shrub coverage classes, respectively (solid circles). Interestingly, ADM anisotropic factors for individual IGBP scene types show a remarkable similarity to one another and to the combined low-to-moderate and moderate-to-high tree/shrub coverage classes. In **Figure 5**, deviations in anisotropic factors for individual IGBP types from the moderate-to-high tree/shrub ADM class occur primarily in angular bins that are poorly sampled. This is particularly evident for the Closed Shrubs (6) and Mixed Forest (5) IGBP types. The most persistent differences between anisotropic factors from the individual IGBP types and the combined low-to-moderate tree/shrub coverage class occur close to nadir: Grassland (10) anisotropic factors are generally larger by up to 4% (relative difference), whereas anisotropic factors for Crops (12) are generally lower by up to 3%. Differences also increase at larger viewing zenith angles, where the data sampling is reduced (note that since the CERES SSF only retains footprints within the VIRS swath, oblique viewing zenith angles are only sampled when CERES is in RAP or alongtrack mode, which only occurs every third day of data acquisition).

To reduce errors in flux due to poorly sampled ADM angular bins, the CERES ADMs are constructed using the low-to-moderate and moderate-to-high tree/shrub coverage classes to determine fluxes over land. For these cases, the variability in the anisotropic factors is estimated to be < 0.04 at the 95% confidence level for most solar zenith and viewing zenith angle bins. The variability in anisotropic factors is estimated from the variability in daily mean radiances for each angular bin (Eq. (13)).

ADM anisotropic factors for θ_o =30°-40° for two IGBP types characteristic of desert regions are presented in **Figure 7**. Open Shrubs (7) are prevalent over West and Central Australia, the southwest parts of North America, South America, Africa, and in Central Asia.

Barren Deserts (16) are associated primarily with the Saharan, Arabian, Thar and Gobi deserts. As shown in **Figure 7**, ADMs are quite different for these two IGBP types. The ADMs over Barren Desert regions are more isotropic, presumably due to the lower vegetation coverage there. Capderou (1998) showed similar differences based on Scanner for Radiation Budget (ScaRaB) measurements from the Meteor-3-07 satellite.

To examine how well the IGBP classification separates the two classes of desert, relative frequency distributions of SW reflectance were determined in each angular bin. SW reflectance is inferred from a measured SW radiance as follows:

$$r(\theta_o, \theta, \phi; h_{sfc}) = \frac{\pi I(\theta_o, \theta, \phi; h_{sfc})}{\mu_o E_o} \left(\frac{d}{d_o} \right)^2 \times 100\% \tag{20}$$

where $\mu_o = \cos\theta_o$, E_o is the incident solar irradiance (=1365 W m^{-2}), d corresponds to the Earth-sun distance at the time of observation, and d_o is the mean Earth-sun distance.

Figure 8 shows results for angular bin θ_o=40°-50°, θ=0°-10° and ϕ=70°-90°. While the two desert types have a well-defined primary peak at reflectances near 15% (Open Shrubs) and 30% (Barren Desert), a secondary peak in the Barren Desert distribution occurs near 15%, and there is a hint of a secondary peak in the Open Shrubs distribution at reflectances near 25%. The reason for the multiple peaks in the two reflectance distributions may be because the fixed IGBP map cannot account for annual or seasonal changes in vegetation type and cover. To provide a better separation between the two desert types, all CERES footprints in 10' desert regions are reclassified as either "Dark" or "Bright" desert. Regions with CERES SW reflectances closer to the primary peak of the Open Shrubs reflectance distribution are classified as "Dark Desert", whereas regions with CERES SW reflectances closer to the primary peak of the Barren Desert reflectance distribution are classified as "Bright Desert".

The largest difference in ADM characteristics between the reclassified desert ADMs (Dark and Bright Desert) from the original IGBP classes (Open Shrubs and Barren Deserts) occurs for the Bright Desert class. In that case, the Bright Desert ADMs are more isotropic than the Barren Desert ADMs, particularly in the forward scattering direction, where differences in anisotropic factors can reach 6%. In addition, for both desert types, the ADM variability estimate (Eq. (13)) is much smaller for the new Dark and Bright desert classes. For these cases, the variability in the anisotropic factors is estimated to be < 0.03 at the 95% confidence level for most solar zenith and viewing zenith angle bins.

Recently, Capderou (1998) constructed clear desert ADMs using measurements from the Scanner for Radiation Budget (ScaRaB) instrument on board the *Meteor-3-07* satellite. Using scene identification based on the ERBE Maximum Likelihood Estimation (MLE) technique (Wielicki and Green, 1989) to identify clear scenes over the Saharan, Arabian, Namib-Kalahari, and Australian deserts, Capderou (1998) derived ADMs for "dark" and "bright" desert conditions. To compare the ScaRaB and CERES ADMs, the CERES ADMs are adjusted to the midpoint of the ScaRaB ADM angular bins (ScaRaB uses the same angular bin definitions as ERBE) by interpolating CERES ADM mean radiances ($\bar{I}_j^{SW}$) and fluxes (F_j^{SW}) to the angular bin midpoints and inferring the anisotropic factors from the ratio. The ScaRaB-CERES ADM differences are converted to equivalent SW flux differences by inferring fluxes from the CERES ADM mean radiances ($\bar{I}_j^{SW}$) using both sets of ADMs in each ScaRaB ADM angular bin ($\theta >$ 75° excluded) as though the radiances were instantaneous values. **Figure 9** shows the resulting SW flux differences and root-mean-square (RMS) differences as a function of solar zenith angle inferred from all angular bins. Also provided are results comparing fluxes based on ERBE (Suttles et al., 1988) and CERES desert ADMs. For solar zenith angle bins < 60°, the ScaRaB

and ERBE fluxes are generally within 3 W m^{-2} of the CERES fluxes for both the dark and bright desert models. At larger solar zenith angles, both the ScaRaB and ERBE fluxes are lower than the CERES fluxes by up to 7 W m^{-2}.

The cause for the increase in flux difference with solar zenith angle is unclear. Further examination of the ScaRaB and ERBE ADMs reveals some large jumps in the nadir anisotropic factors at solar zenith angles > 60°. **Figure 10a-h** show the CERES, ScaRaB and ERBE ADM anisotropic factors for the θ=0°-15° ERBE angular bin against solar zenith angle in each of the ERBE relative azimuth angle bins. While the CERES anisotropic factors show a smooth dependence on solar zenith angle, the ScaRaB and ERBE models are much noisier, particularly at the larger solar zenith angles. The cause for the large variability in the ScaRaB and ERBE models may be due to poor sampling or possibly a solar zenith angle dependent bias in the MLE scene identification.

6.3 Clouds Over Ocean

The ADM scene type stratification for clouds over ocean is provided in **Table 2**. There are two phase categories, 12 cloud fraction categories, and 14 cloud optical depth categories. Phase over a CERES footprint is inferred from VIRS imager pixel-level phase retrievals (Minnis et al., 1998). Each VIRS imager pixel within a CERES cloud layer is assigned a phase index of 1 for liquid water and 2 for ice. The pixel-level phase indices are weighted by the CERES PSF to yield the effective phase over each layer. The effective phase over the entire footprint is determined by area-averaging the phase indices of each layer using Eq. (1). ADMs for "liquid clouds" are determined from footprints with an effective phase index < 1.5, and ADMs for "ice clouds" are determined from footprints with an effective phase index ≥ 1.5. While a separate

class for "mixed-phase" footprints would be desirable, the sampling is limited with only 9 months of CERES/TRMM observations.

Although the number of ocean cloud ADM scene types can potentially reach 336 (i.e., 2×12×14), the actual number of scene types with sufficient data is much lower. In most solar zenith angle bins, 72 (or 43%) of the possible liquid water cloud classes have sufficient data to build an ADM, whereas 57 (or 34%) of the possible ice cloud classes have sufficient sampling. **Figure 11**(a) and **Figure 11**(b) show the frequency of occurrence of liquid water and ice cloud ADM classes, respectively, by cloud fraction and cloud optical depth. When cloud fraction is low, only the thin ADM cloud classes are sampled. As the cloud fraction increases, the range in cloud optical depth increases, and more cloud optical depth ADM classes appear. A similar broadening in cloud optical depth distributions with cloud cover was also observed by Barker et al. (1996).

When clouds are present, 37% of the footprints fall in the overcast (99.9-100%) cloud fraction class. If only footprints dominated by liquid water clouds (i.e. footprint effective phase index < 1.5) are considered, the fraction of overcast footprints drops to 25%, compared to 72% for footprints dominated by ice clouds (i.e. footprint effective phase index $\geq$ 1.5). Overall, the frequency of occurrence for the liquid water cloud class is 75%, compared to 25% for the ice cloud class.

Examples of ADMs for thin (cloud optical depths 1.0-2.5) and thick (cloud optical depths 20-25) ice clouds for θ_o=50°-60° are provided in **Figure 12a-b**. For the thin cloud case (**Figure 12a**), the anisotropic factor ranges from 0.6 to 3.3 compared to 0.9 to 1.6 for the thick cloud case. The largest sensitivity to cloud optical depth occurs at near-nadir views, where the anisotropic factor changes by 50%. **Figure 12c-d** show differences in anisotropic factors between liquid

water and ice cloud ADMs for the same cloud optical depth intervals as in **Figure 12a-b**. For both the thin (**Figure 12c)** and thick **(Figure 12d**) cloud conditions, anisotropic factors for liquid water clouds exceed those of ice clouds in the forward and backscattering directions, but are smaller at relative azimuth angles in the side scattering direction. A similar dependence was observed from POLarization and Directionality of the Earth's Reflectances (POLDER) measurements by Loeb et al. (2000). As expected, the magnitude of the differences is smaller for the thicker cloud case **(Figure 12d**) since increased multiple scattering in these clouds reduces the sensitivity to differences in liquid water and ice cloud phase functions. However, because albedos and fluxes are so much larger for thicker clouds, even small errors in anisotropy can cause large albedo errors. For the cloud cases shown in **Figure 12**, ignoring phase would result in mean albedo errors of up to 0.05.

Figure 13 compares CERES ADMs for overcast ice clouds for each of the 14 cloud optical depth intervals together with the one ERBE overcast ADM. For this comparison, the CERES ADMs are interpolated to the midpoints of the ERBE angular bins (Suttles et al., 1988). The ERBE overcast model most closely follows the CERES ADM for cloud optical depth interval 12.5-15. The ERBE anisotropic factors exceed CERES values by up to 60% for thin clouds near nadir, while for viewing zenith angles between 40° and 60°, anisotropic factors are rather insensitive to cloud optical depth, consistent with theoretical simulations by Davies (1984).

Because of the strong sensitivity in the anisotropic factors to cloud properties (i.e., cloud optical depth and cloud fraction), the ADM look-up tables under cloudy conditions are interpolated not only to the measurement viewing geometry, but also to the effective cloud

fraction and cloud optical depth over the footprint. The interpolation procedure is the same as that outlined in **Section 5.1** but involves interpolation over two extra variables.

6.4   Clouds Over Land

The ADM classes for cloudy conditions over land are stratified by the four land types considered for clear conditions (**Section 6.2**), 2 cloud phase classes (defined in the same manner as for clouds over ocean), 5 cloud fraction classes and 6 cloud optical depth classes (**Table 2**). Since only 9 months of CERES/TRMM measurements are available, the number of classes over each of the land types is reduced relative to that over ocean in order to ensure a sufficient number of samples to construct an ADM.

6.5   Snow

Since the TRMM orbit is restricted to 35°S-35°N, sampling under snow conditions is insufficient for developing empirical ADMs. As an alternative, fluxes under snow conditions for CERES/TRMM are determined from theoretical ADMs based on twelve-stream DISORT (Stamnes et al., 1988) radiative transfer model calculations. In the calculations, the surface bidirectional reflectance of snow is accounted for explicitly by inserting a packed snow layer at the bottom of the atmosphere (0 to 1 km altitude). Within the snow layer, ice particles are assumed to be spheres, having a lognormal size distribution with a mode radius of 50 μm and a standard deviation of 2.0 μm. The concentration of ice particles is 1.0×10^{12} m^{-3}, which corresponds to a density of ≈ 0.5 M g m^{-3}. Ice refractive indices from Warren (1984) are used to compute the optical properties of ice particles from Mie theory. The atmosphere is divided into 6 layers. Absorption by water vapor, ozone, carbon dioxide, and oxygen are based on *k*-

distribution tables (Kato et al., 1998) assuming a Midlatitude Summer atmosphere (McClatchey et al., 1972).

Under cloudy conditions, a liquid water cloud layer between 1 and 2 km is inserted above the snow layer in the DISORT model calculations. The cloud particles are also taken to be spheres, having a lognormal distribution with a mode radius of 10 μm and standard deviation of 1.42 μm. The cloud optical depth is fixed at 10. Radiances are computed at 18 solar zenith angles, 51 viewing zenith angles and 61 relative azimuth angles. TOA fluxes from the theoretical ADMs are determined using Eq. (14).

7. LW and WN ADM Scene Types

For CERES, LW and WN ADMs are defined independently of the SW ADMs. This approach differs from that of ERBE, which uses the same scene types for both the SW and LW ADMs. CERES LW and WN ADMs are determined for scene types defined by meteorological parameters and imager-based cloud parameters that influence LW and WN radiance anisotropy of Earth scenes. As a result, the ERBE method of defining LW ADMs by colatitude is not used in CERES since latitudinal and seasonal variations in anisotropy are accounted for on a footprint-by-footprint basis from collocated meteorological and imager-based parameters. Also, since the cloud retrieval algorithm uses a different method at night than it does during the daytime, CERES ADMs are determined separately for daytime and nighttime conditions.

The LW and WN ADMs are divided into broad categories based on cloud cover (clear, broken and overcast) and surface type (ocean, land and desert). Each of these categories is further stratified by intervals of precipitable water, cloud fraction, vertical temperature change and cloud infrared emissivity (**Table 3**). To ensure that there is sufficient sampling for every scene type, the parameters are stratified according to their frequency distributions using fixed

percentile intervals rather than fixed discrete intervals. The percentile approach allows the data to define the width and range used to stratify a given parameter, thereby ensuring that each ADM scene type is adequately sampled.

7.1 LW and WN ADM Scene Type Parameters

Cloud categories are based on the imager-derived cloud fraction over the CERES footprint. A footprint is assumed to be clear when the cloud fraction ≤ 0.1%, "Broken" when the cloud fraction is between 0.1% and 99.9%, and "Overcast" when the cloud fraction ≥ 99.9%. In **Table 3**, ocean is defined by IGBP type 17 (**Table 1**), Desert is defined by IGBP types 7 and 16, and Land is all IGBP types except 7, 15, 16, 17, 19 and 20. Over snow, empirically-derived LW and WN ADMs are unavailable because of inadequate sampling. Therefore, fluxes for footprints over snow are estimated in the same manner as footprints with insufficient imager information (**Section 5.3**).

Precipitable water in **Table 3** is the water vapor burden from the surface to the TOA. For scenes over water, the data source for precipitable water is the SSM/I dataset, if available. If SSM/I data are unavailable or the footprint is over land, ECMWF precipitable water is used. Under clear conditions, the vertical temperature change (ΔT_s) corresponds to the lapse rate in the first 300 hPa of the atmosphere above the surface. It is computed by subtracting the air temperature at the pressure level 300 hPa below the surface (i.e., surface pressure minus 300 hPa) from the imager-based surface skin temperature. A separate ADM class is produced when there is an inversion in the boundary layer ($\Delta T_s < 0°C$). When clouds are present in a CERES footprint, vertical temperature change (ΔT_c) refers to the difference in temperature between the surface and cloud. ΔT_c is computed by subtracting the imager-based effective (equivalent blackbody) cloud layer temperature from the underlying skin temperature. If the

imager-based surface skin temperature is unavailable (e.g., overcast conditions), a skin temperature from the ECMWF data assimilation model is used.

The mean infrared emissivity for a cloud layer is defined as the ratio of the difference between the observed and clear-sky VIRS 11-μm radiances to the difference between the cloud emission and clear sky radiances. The clear-sky radiance is determined either from surrounding cloud-free observations when available, or from ECMWF surface skin temperature, surface emissivity maps, and ECMWF vertical profiles of temperature and humidity. The cloud emission radiance is defined as the blackbody radiance at the radiating temperature of the cloud. The mean infrared emissivity, cloud radiating temperature and effective particle size are determined using an iterative procedure that minimizes the difference between calculated and observed VIRS radiances in the visible, solar-infrared and infrared channels. The procedure relies on parameterizations described in Minnis et al. (1998) to relate cloud optical depth, particle size and cloud infrared emissivity. Because scattering tends to block radiation from the warmer, lower portions of the cloud, the observed radiance can be less than the cloud emission radiance (i.e., the cloud appears colder than it really is). In these cases the effective emissivity will be greater than one. This occurs most often for optically thick clouds at large imager viewing zenith angles, and for FOVs containing optically thick clouds that have an equivalent blackbody temperature that is within a few degrees of the clear-sky temperature (Minnis et al., 1998).

7.2   ADM Sensitivity to Scene Type

Figure 14 provides examples of LW and WN ADMs for clear scenes over ocean, land and desert as a function of ΔT_s for the 33-66th percentile interval of precipitable water. The ΔT_s intervals correspond to the 0-25, 25-50, 50-75, and > 75 percentile intervals (there wasn't sufficient sampling to construct ADMs for inversion conditions). The range of ΔT_s is much

smaller over ocean than it is over land and desert because ΔT_s has a much narrower distribution over ocean. As ΔT_s increases, LW and WN anisotropy increases. For $\theta < 70°$, the largest sensitivity in the LW anisotropic factors to ΔT_s occurs close to nadir, where it varies by $\approx 2\%$, which corresponds to a LW flux variation of ≈ 6 W m^{-2}. Sensitivity to ΔT_s is more pronounced for the WN channel because of its larger dependence on surface temperature.

LW and WN anisotropies change between daytime and nighttime conditions over clear desert regions (**Figure 15**a-d). Because daytime surface temperatures are so much larger than those at night, the magnitude of ΔT_s in each percentile interval is greater during the daytime (**Table 4**). Consequently, the daytime LW and WN anisotropy is stronger than at night. Based on these results, ignoring daytime/nighttime differences in anisotropy would lead to a 5 W m^{-2} bias in the day/night LW flux difference.

In broken cloud conditions, LW anisotropy shows a slight dependence on cloud infrared emissivity (**Figure 16).** Sensitivity to ε increases with cloud cover and cloud height, particularly over moist land. In general, LW anisotropy increases with decreasing ε. This trend is most pronounced for overcast conditions, as illustrated in **Figure 17**, which shows nadir anisotropic factors for low and high overcast clouds. Clouds occurring in the wettest (largest precipitable water) regions with the largest ΔT_c show the strongest sensitivity to ε. Anisotropic factors range from 1.02 for thick high clouds to 1.158 for thin high clouds in the moist regions. This $\approx 13\%$ difference in anisotropic factor corresponds to a difference in LW flux of 25 W m^{-2} for these clouds.

8. Summary

The new generation of radiation budget products from CERES merges SW, LW and WN TOA radiative fluxes from the CERES instrument with coincident imager-derived cloud and aerosol parameters and meteorological information from the European Centre for Medium-Range Weather Forecasts (ECMWF) data assimilation analysis. Conversion of measured broadband radiances to TOA radiative fluxes requires models of the angular dependence of reflected and emitted radiance under all atmospheric and surface conditions. CERES uses coincident broadband and narrowband imager measurements to construct Angular Distribution Models (ADMs) that are functions of scene type parameters that have a strong influence on the anisotropy (or angular variation) of the Earth's radiation field at the TOA. The CERES/TRMM ADMs are constructed from 9 months of CERES and VIRS imager measurements from the TRMM spacecraft, which has a 35° inclined orbit between 35°S and 35°N. Because of TRMM's unique orbit, the ADMs are based on measurements that cover the full range of solar zenith angles over the Tropics.

For clear scenes, CERES/TRMM SW ADMs are defined over ocean, land and desert, while theoretical ADMs are used over snow. Clear-sky ocean models are a function of wind speed, and use a theoretical adjustment to account for aerosol optical depth variations. Over land, ADMs are divided into two classes: moderate-to-high tree/shrub coverage and low-to-moderate tree/shrub coverage. ADMs for individual IGBP types belonging to these two categories show a remarkable similarity, although albedos are quite different. Desert ADMs are defined for dark and bright desert regions by slightly modifying the Open Shrub and Barren Desert IGBP types based on SW reflectance relative frequency distributions. The new Desert ADMs are similar to models developed by Capderou (1998) using ScaRaB data, except at larger solar zenith angles

where differences between the ScaRaB and CERES ADMs lead to flux differences of up to 7 W m^{-2}. ADMs for cloudy conditions are defined for several classes stratified by surface type, cloud fraction, cloud phase, and cloud optical depth. ADM sensitivity to cloud optical depth and phase are shown to be particularly important. For example, variations in anisotropy as a function of cloud optical depth can be as large as 50%.

LW and WN ADMs are provided as a function of viewing zenith angle for scene types defined by surface type, cloud fraction, precipitable water, lapse rate and cloud infrared emissivity. To ensure sufficient data for all angular bins and scene types, the parameters are stratified according to their frequency distributions using fixed percentile intervals rather than fixed discrete intervals. The largest sensitivity to the various ADM scene type parameters occurs at nadir viewing zenith angles. In general, the anisotropy over moist land regions is larger than over ocean, both in clear and cloudy conditions. LW and WN anisotropies increase with precipitable water and atmospheric lapse rate for clear scenes, while it increases with cloud cover, the difference between surface and cloud-top temperature and decreasing cloud infrared emissivity for cloudy scenes.

Acknowledgements

Appendix

Under sampled ADM angular bins are estimated from a combination of the observed radiances in angular bins where sampling is adequate, and radiative transfer model simulations drawn from a theoretical database. The specific model simulation selected from the database is that which most closely resembles the bidirectional reflectance of the observations in angular bins where data are available. The procedure, described in Section 4, is used mainly to fill in missing data angular bins between 80° and 90° (at the surface reference level). At viewing zenith angles beyond the Earth's tangent point, MODTRAN simulations for a molecular atmosphere are used. This section describes the radiance model database used to estimate radiances in missing angular bins that intersect the Earth.

SW Radiative Transfer Model Database

SW radiative transfer calculations are based on the DISORT radiative transfer code (Stamnes et al., 1988). Radiances are determined at 36 viewing zenith angles both at the top and bottom of the atmosphere, 19 relative azimuth angles, and 18 solar zenith angles. A minimum of 16 streams are used in clear conditions, and a minimum of 48 streams are used for cloudy conditions. The calculations are performed at 40 wavelengths. Molecular transmission at each wavelength is based on the MODTRAN 3.7 model (Kneizys et al., 1996). The atmosphere is divided into four homogeneous layers consisting of a boundary layer, a cloud layer, a tropospheric layer and a stratospheric layer. Contributions from a surface bidirectional reflectance model is included explicitly (outside of DISORT) by adding the surface direct and surface diffuse radiance contributions to the TOA radiance contribution from the atmosphere determined by DISORT. With this approach, several different surface bidirectional reflectance

models can be coupled with the same DISORT result, thereby reducing the number of DISORT runs needed.

Table A.1 summarizes the input parameters used in the radiative transfer model calculations. Clear conditions over ocean assume a Maritime Tropical aerosol (Hess et al., 1998) and an ocean surface bidirectional reflectance at five wind speeds using the "OCEABRDF" subroutine from the 6S radiative transfer code (Vermote et al., 1997). This routine accounts for specular reflection (Cox and Munk, 1954), wind-speed dependent whitecaps (Koepke, 1984), and below water surface reflectance (Morel, 1988). For clear land and desert, the Continental Average and Desert aerosol models of Hess et al. (1998) are used. Surface bidirectional reflectance measurements of Kriebel (1977) over Forest, Grass and Savannah, and the parameterizations of Ahmad and Deering (1992) over Alkali Flat, Bare Field, Prairie and Desert, are used to model surface bidirectional reflectances over land and desert. Liquid water clouds are modeled using the Stratus (maritime) model of Hess et al. (1998). Ice clouds are comprised of a mixture of crystal habits including bullet rosettes, aggregates and hollow columns (Yang et al., 2000) with a size distribution given by the "Ci (Cold)" case described in Baum et al. (2000).

To simulate the bidirectional reflectance of broken clouds, the clear and cloudy radiances at each angle are linearly weighted by cloud fraction. The specific cloud fractions used correspond to the midpoint of the ADM cloud fraction intervals (**Table 2**).

LW and WN Radiative Transfer Model Database

LW and WN radiative transfer calculations are based on a radiative transfer code by Gupta et al. (1985). The model determines broadband radiances over the 5-50 μm range with a 10 cm^{-1} resolution. Atmospheric transmittance in each spectral interval is calculated using a quasi-random band model (Wyatt et al., 1962), with spectral parameters based on the line

parameter compilation of McClatchey (1973), and continuum absorption by water vapor based on Roberts et al. (1976). The model consists of 15 atmospheric layers between the surface and 10 hPa. Atmospheric profiles include the U.S. standard atmosphere, the tropical, midlatitude summer/winter and subarctic summer/winter atmospheric profiles of McClatchey et al. (1972), and atmospheric profiles from 1-year global NOAA-6 and NOAA-7 TOVS datasets over the Tropical Western Pacific, Amazon, Saudi Arabia, North Atlantic, Midlatitude U.S., North Sea, Northern Canada and Antarctica. Cloud top heights in each location are specified at four levels, depending on the location. Broken clouds are simulated by linearly weighting the clear and overcast radiances.

References

Ahmad, S. P., and D. W. Deering, 1992: A simple analytical function for bidirectional reflectance. *J. Geophys. Res.*, **97**, 18,867-18,886.

Barker, H.W., B.A. Wielicki, and L. Parker, 1996: A parameterization for computing grid-averaged solar fluxes for inhomogeneous marine boundary layer clouds. Part II: Validation using satellite data. *J. Atmos. Sci.*, 53, 2304-2316.

Barkstrom, B.R., 1984: The Earth Radiation Budget Experiment (ERBE). *Bull. Amer. Meteorol. Soc.*, **65**, 1170-1186.

Baum, B. A., D. P. Kratz, P. Yang, S. C. Ou, Y. Hu, P. F. Soulen, and S.-C. Tsay, 2000: Remote sensing of cloud properties using MODIS airborne simulator imagery during SUCCESS. Part I: Data and models. *J. Geophys. Res.*, **105**, 11,767-11,780.

Baum, B. A., P. Yang, and A. Heymsfield, 1999: Overlapping cloud layer detection and analysis using MODIS Airborne Simulator imagery. *Proc. AMS 10th Conf. Atmos. Rad.*, Madison, WI, June 28-July 2, 230-233.

Belward, A., and T. Loveland, 1996: The DIS 1km Land Cover Data Set, *GLOBAL CHANGE, The IGBP Newsletter*, **#27**, Sep., 1996.

Buriez, J.C., C. Vanbauce, F. Parol, P. Goloub, M. Herman, B. Bonnel, Y. Fouquart, P. Couvert, and G. Sèze, 1997: Cloud detection and derivation of cloud properties from POLDER. *Int. J. Remote Sens.*, **18**, 2785-2813.

Capderou, M., 1998: Determination of the shortwave anisotropic function for clear-sky desert scenes from ScaRaB data: Comparison with models issued from other satellite data. *J. Appl. Meteor.*, **37**, 1398-1411.

Chambers, L. H., B. A. Wielicki, and N. G. Loeb, 2001: Shortwave flux from satellite-measured radiance: A theoretical study over marine boundary layer clouds. J. Appl. Meteor., 40, 2144-2161.

Chang, F.-L., Z. Li, and A. P. Trishchenko, 2000: The dependence of TOA reflectance anisotropy on cloud properties inferred from ScaRaB satellite data, *J. Appl. Meteor.*, **39**, 2480-2493.

Chen, Y., S. Sun-Mack, P. Minnis, W. L. Smith, Jr., and D. F. Young, 1999: Surface emissivity derived for infrared remote sensing from satellites. *Proc. AMS 11th Conf. on Satellite Meteorology and Oceanography*, Madison, WI, Oct 15-18, 512-515.

Cox, S.K., D.S. McDougal, D.A. Randall, and R.A. Schiffer, 1987: FIRE—The First ISCCP Regional Experiment. *Bull. Amer. Meteor. Soc.*, **68**, 114-118.

Cox, C., and W. Munk, 1954: Some problems in optical oceanography, *J. Mar. Res.*, **14**, 63-78.

Davies, R., 1984: Reflected solar radiances from broken cloud scenes and the interpretation of scanner measurements, *J. Geophys. Res.*, **89**, 1259-1266

Di Girolamo, L., T. Varnai and R. Davies, 1998: Apparent breakdown of reciprocity in reflected solar radiances *J. Geophys. Res.*, **103**, 8795-8803.

Diner, D. J., G. P. Asner, R. Davies, Y. Knyazikhin, J.-P. Muller, A. W. Nolin, B. Pinty, C. B. Schaaf, and J. Stroeve, 1999: New Directions in Earth Observing: Scientific Applications of Multiangle Remote Sensing. *Bulletin of the American Meteorological Society*: **80**, 2209–2228.

Geier, E.B., R. N. Green, D. P. Kratz, P. Minnis, W. F. Miller, S. K. Nolan, and C. B. Franklin, 2001: Single satellite footprint TOA/surface fluxes and clouds (SSF) collection document. [available on-line from http://asd-www.larc.nasa.gov/ceres/ASDceres.html.]

Geogdzhayev, I. V., M. I. Mishchenko, W. B. Rossow, B. Cairns, and A. A. Lacis, 2002: Global two-channel AVHRR retrievals of aerosol properties over the ocean for the period of NOAA-9 observations and preliminary retrievals using NOAA-7 and NOAA-11 data. *J. Atmos. Sci.*, **59**, 262-278.

Goodberlet, M., C. Swift, and J. Wilkerson, Ocean surface wind speed measurements of Special Sensor Microwave/Imager (SSM/I), IEEE Geosci. Rem. Sen., GE-28, 828-832, 1990.

Gupta, S. K., S. N. Tiwari, C. S. Vemuru, and J. T. Suttles, 1985: Infrared limb-darkening effects for the Earth-atmosphere system. *AIAA Journal*, **23**, 405-409.

Hess, M., P. Koepke, and I. Schult, 1998: Optical properties of aerosols and clouds: The software package OPAC. *Bull. Amer. Meteor. Soc.*, **79**, 831-844.

Ignatov, A., 1997: Estimating aerosol phase function in backscatter from AVHRR and sun-photometer measurements. *J. Appl. Meteor.*, **36**, 688-694.

Ignatov, A. and L. L. Stowe, 2002: Aerosol retrievals from individual AVHRR channels: I. Retrieval algorithm and transition from Dave to 6S radiative transfer model. *J. Atm. Sci.*, **59**, 313-334.

Kandel, R., M. Viollier, P. Raberanto, J. Ph. Duvel, L.A. Pakhomov,V.A. Golovkp, A.P. Trishchenko, J. Mueller, E. Raschke, R. Stuhlmann, and the International ScaRaB Scientific Working Group (ISSWG), 1998: The ScaRaB earth radiation budget dataset. *Bull. Amer. Meteor. Soc.*, **79**, 765-783.

Kato, S., T. P. Ackerman, J. H. Mather, and E. E. Clothiaux, 1999: The *k*-distribution method and correlated-*k* approximation for a shortwave radiative transfer model, *J. Quant. Spec. Rad. Tran.*, **62**, 109-121.

Koepke, P., 1984: Effective reflectance of oceanic whitecaps. Appl. Optics, 23, 1816-1822.

Kriebel, K. T., 1977: Reflection properties of vegetated surfaces: tables of measured spectral biconical reflectance factors, Munich University Meteorologisches Inst., Wissenschaftilche, Mitteilung, 84 pp.

Kummerow, C., W. Barnes, T. Kozu, J. Shiue, and J. Simpson, 1998: The Tropical Rainfall Measuring Mission (TRMM) sensor package. *J. Atmos. Ocean. Tech.*, **15**, 809-817.

Li, X., S. A. Christopher, J. Chou, and R. M. Welch, 2000: Estimation of shortwave direct radiative forcing of biomass-burning aerosols using new angular models. *J. Appl. Meteor.*, **39**, 2278-2291.

Loeb, N. G., F. Parol, J.-C. Buriez, and C. Vanbauce, 2000: Top-of-atmosphere albedo estimation from angular distribution models using scene identification from satellite cloud property retrievals. *J. Climate,* **13**, 1269-1285.

Loeb, N. G., K. J. Priestley, D. P. Kratz, E. B. Geier, R. N. Green, B. A. Wielicki, P. O'R. Hinton, and S. K. Nolan, 2001: Determination of unfiltered radiances from the Clouds and the Earth's Radiant Energy System (CERES) instrument. *J. Appl. Meteor.,* **40**, 822-835.

Loeb, N. G., S. Kato, and B. A. Wielicki, 2002: Defining top-of-atmosphere flux reference level for Earth radiation budget studies. *J. Climate* (in press).

Manalo-Smith, N., and N. G. Loeb, 2001: Longwave and window angular distribution models from CERES/TRMM radiance measurements. *Proc. AMS 11th Conf. on Satellite Meteorology and Oceanography*, Madison, WI, Oct 15-18, 122-125.

McClatchey, R. A., et al., 1973: AFCRL atmospheric absorption line parameters compilation. AFCRL-TR-73-0096.

McClatchey, R. A., R. W. Fenn, J. E. A. Selby, F. E. Volz, and J. S. Garing, 1972: Optical properties of the atmosphere. AFCRL-72-0497.

Minnis, P., D. P. Garber, D. F. Young, R. F. Arduini, and Y. Tokano, 1998: Parameterizations of reflectance and effective emittance for satellite remote sensing of cloud properties. *J. Atmos. Sci.*, **55**, 3313-3339.

Minnis, P., and M. M. Khaiyer, 2000: Anisotropy of land surface skin temperature derived from satellite data. *J. Appl. Meteor.*, **39**, 1117-1129.

Minnis, P., D. P. Kratz, J. A. Coakley, Jr., M. D. King, D. Garber, P. Heck, S. Mayor, D. F. Young, and R. Arduini, 1995: Cloud Optical Property Retrieval (Subsystem 4.3). "Clouds and the Earth's Radiant Energy System (CERES) Algorithm Theoretical Basis Document, Volume III: Cloud Analyses and Radiance Inversions (Subsystem 4)", *NASA RP 1376 Vol. 3*, edited by CERES Science Team, pp. 135-176.

Minnis., P., D. F. Young, B. A. Wielicki, P. W. Heck, X. Dong, L. L. Stowe, and R. Welch, 1999: CERES cloud properties derived from multispectral VIRS data. *Proc. the EOS/SPIE Symposium on Remote Sensing*, **3867**, Florence, Italy, September 20-24, 1999, 91-102.

Morel, A., 1988: In-water and remote measurements of ocean color. *Boundary-Layer Meteor.*, **18**, 177-201.

Priestley, K. J., R. B. Lee III, R. N. Green, S. Thomas, and R.S. Wilson, 1999: Radiometric performance of the Clouds and the Earth's Radiant Energy System (CERES) proto-flight model on the Tropical Rainfall Measuring Mission (TRMM) spacecraft for 1998. *Proc. AMS 10th Conf. Atmos. Rad.*, Madison, WI, June 28-July 2, 33-36.

Rabier, F., J.-N. Thepaut, and P. Courtier, 1998: Extended assimilation and forecast experiments with a four-dimensional variational assimilation. *Quart. J. Roy. Meteor. Soc.*, **124**, 1861-1887.

Roberts, R. E., J. E. A. Selby, and L. M. Biberman, 1976: Infrared continuum absorption by atmospheric water vapor in the 8-12 mμ window. *Appl. Opt.*, **15**, 2085-2090.

Rossow, W.B., and R.A. Schiffer, 1991: ISCCP cloud data products, *Bull. Amer. Meteor. Soc.*, **72**, 2-20.

Roujean, J.-L., M. Leroy, P.-Y. Deschamps, 1992: A bidirectional reflectance model of the Earth's surface for the correction of remote sensing data. *J. Geophys. Res.*, **97**, 20,455-20,468.

Smith, G. L., 1994: Effects of time response on the point spread function of a scanning radiometer. *Appl. Opt.*, **33**, 7031-7037.

Stamnes, K., S.-C. Tsay, W. Wiscombe, and K. Jayaweera, 1988: Numerically stable algorithm for discrete-ordinate-method radiative transfer in multiple scattering and emitting layered media. *Appl. Opt.*, **24**, 2502-2509.

Stowe, L., R. Hucek, P. Ardanuy, and R. Joyce, 1994: Evaluating the design of an Earth radiation budget instrument with system simulations. Part II: Minimization of instantaneous sampling errors for CERES-I, *J. Atmos. Ocean Tech.*, **11**, 1169-1183.

Sun-Mack, S., Y. Chen, T. D. Murray, P. Minnis, and D. F. Young, 1999: Visible clear-sky and near-infrared surface albedos derived from VIRS data for CERES. *Proc. AMS 10th Conf. Atmos. Rad.*, Madison, WI, June 28-July 2, 422-425.

Suttles, J.T., R.N. Green, P. Minnis, G.L. Smith, W.F. Staylor, B.A. Wielicki, I.J. Walker, D.E. Young, V.R. Taylor, and L.L. Stowe, 1988: Angular radiation models for Earth-atmosphere systems, Vol. I─shortwave radiation. *Rep. NASA RP-1184*, NASA, Washington, D.C.

Suttles, J.T., R.N. Green, G.L. Smith, B.A. Wielicki, I.J. Walker, V.R. Taylor, and L.L. Stowe, 1989: Angular radiation models for Earth-atmosphere systems, Vol. II─longwave radiation. *Rep. NASA RP-1184*, NASA, Washington, D.C.

Trepte, Q., Y. Chen, S. Sun-Mack, P. Minnis, D. F. Young, B. A. Baum, and P. W. Heck, 1999: Scene identification for the CERES cloud analysis subsystem. *Proc. AMS 10th Conf. Atmos. Rad.*, Madison, WI, June 28-July 2, 169-172.

Vermote, E., D. Tanré, J.L. Deuzé, M. Herman, and J.J. Morcette, 1997: Second simulation of the satellite signal in the solar spectrum: An overview. *IEEE Transactions on Geoscience and Remote Sensing*, **35**, 675-686.

Warren, S. G., 1984: Optical constants of ice from the ultraviolet to the microwave, *Appl. Opt.*, **23**, 1206-1225.

Welch, R. M., S. K. Sengupta, A. K. Goroch, R. Palikonda, N. Rangaraj, and M. S. Navar, 1992: Polar cloud and surface classification using AVHRR imagery—An intercomparison of methods. *J. Appl. Meteor.*, **31**, 405-420.

Wielicki, B.A., R. D. Cess, M. D. King, D. A. Randall, and E. F. Harrison, 1995: Mission to planet Earth: Role of clouds and radiation in climate. *Bull. Amer. Meteor. Soc.*, **76**, 2125-2152.

Wielicki, B.A., and R.N. Green, 1989: Cloud identification for ERBE radiation flux retrieval. *J. Appl. Meteor.*, **28**, 1133-1146.

Wyatt, P. J., V. R. Stull, and G. N. Plass, 1962: Quasi-random model of band absorption, *J. Optical. Soc. Amer.*, **52**, 1209-1217.

Yang, P., K.N. Liou, K. Wyser, and D. Mitchell, 2000: Parameterization of the scattering and absorption properties of individual ice crystals. *J. Geophys. Res.*, **105**, 4699-4718.

Zhou, Y., K. C. Rutledge, T. P. Charlock, N. G. Loeb, and S. Kato, 2000: Atmospheric corrections using MODTRAN for TOA and surface BRDF characteristics from high resolution spectroradiometric/angular measurements from a helicopter platform. *Advances in Atmos. Sci.*, **18**, 984-1004.

Figures

Figure 1 Schematic of a CERES footprint showing two cloud layers and a clear region. Two

distinct cloud layers are defined only if their mean effective cloud pressures (denoted by

dashed lines) are statistically different and exceed at least 50 hPa.

Figure 2 Schematic of sun-Earth-satellite viewing geometry.

Figure 3 θ and ϕ angular bin discretization of the CERES/TRMM ADMs.

Figure 4 Schematic of observer viewing geometry at reference level h. Region I corresponds to

Earth views; Region II corresponds to viewing zenith angles between the Earth's tangent

point and the tangent point of a cloud; Region III corresponds to viewing zenith angles that

view the atmosphere above the cloud.

Figure 5 Clear-sky ADM anisotropic factors for θ_o=30°-40° for individual IGBP types with

moderate-to-high tree/shrub coverage. Positive θ corresponds to forward scattering

directions, whereas negative θ corresponds to backscattering.

Figure 6 Same as Figure 5 but for low-to-moderate tree/shrub coverage ADM class.

Figure 7 ADM anisotropic factors at θ_o=30°-40° for Open Shrub and Barren Desert IGBP types.

Figure 8 Reflectance relative frequency distribution for Open Shrub and Barren Desert IGBP

types for angular bin θ_o=40°-50°, θ=0°-10° and ϕ=70°-90°.

Figure 9 SW flux difference over (a) dark desert and (b) bright desert, and RMS SW flux

difference over (c) dark desert and (d) bright desert due to differences between CERES,

ScaRaB and ERBE desert ADMs against solar zenith angle bin midpoint. Solar zenith angle

51

bins are based on the ERBE definition given by: 0°-25.8°, 25.8°-36.9°, 36.9°-45.6°, 45.6°-53.1°, 53.1°-60.0°, 60.0°-66.4°, 66.4°-72.5°, 72.5°-78.5°, 78.5°-84.3°.

Figure 10 Anisotropic factors for θ=0°-15° ERBE angular bin against solar zenith angle for CERES, ScaRaB and ERBE SW ADMs for relative azimuth angle bins (a) 0°-9°; (b) 9°-30°; (c) 30°-60°; (d) 60°-90°; (e) 90°-120°; (f) 120°-150°; (g) 150°-171°; (h) 171°-180°.

Figure 11 Frequency of occurrence of (a) liquid water and (b) ice cloud ADM classes by cloud fraction and cloud optical depth.

Figure 12 Overcast ice cloud ADMs with cloud optical depths between (a) 1.0-2.5 and (b) 20-25 for θ_o=50°-60°. Figure 12c-d show differences in anisotropic factors between liquid water and ice clouds (liquid – ice) for the same cloud optical depth intervals as Figure 12a-b.

Figure 13 SW ADM anisotropic factors interpolated to ERBE angular bins for overcast ice clouds as a function of cloud optical depth, viewing zenith angle and relative azimuth angle for θ_o=53.1-60. Circles correspond to the ERBE overcast ADM.

Figure 14 Daytime clear-sky LW and WN ADMs for the 33-66th percentile interval of precipitable water. ADMs are shown for the LW channel over (a) ocean, (b) land, (c) desert, and for the WN channel over (d) ocean, (e) land, and (f) desert. ΔTs is the vertical temperature difference which corresponds to the lapse rate in the first 300 hPa of the atmosphere above the surface.

Figure 15 LW and WN anisotropic factors for the 0°-10° viewing zenith angle bin over desert as a function of ΔT_s in each precipitable water interval. Anisotropic factors are provided for (a)

daytime LW, (b) nighttime LW, (c) daytime WN, and (d) nighttime WN. Physical values of ΔT_s corresponding to each percentile interval are provided in Table 4.

Figure 16 LW anisotropic factors for the 0°-10° viewing zenith angle bin for broken clouds as a function of cloud emissivity in each cloud fraction interval. (a) Low clouds over dry ocean regions (0-20th ΔT_c percentile interval and 0-33rd precipitable water interval) (b) high clouds over dry ocean regions (80-100th ΔT_c percentile interval and 0-33rd precipitable water interval), (c) low clouds over moist land regions (0-20th ΔT_c percentile interval and 66-100th precipitable water interval), (d) high clouds over moist land regions (80-100th ΔT_c percentile interval and 66-100th precipitable water interval). Physical values corresponding to each percentile interval are provided in Table 5.

Figure 17 LW anisotropic factors for the 0°-10° viewing zenith angle bin for overcast clouds as a function of cloud emissivity in each precipitable water interval. (a) Low clouds (0-20th ΔT_c percentile interval) and (b) high clouds (80-100th ΔT_c percentile interval). Physical values corresponding to each percentile interval are provided in Table 6.

Tables

Table 1 Summary of the IGBP type classification scheme.

Table 2 SW ADM scene type parameter intervals for clouds over ocean, land and desert.

Table 3 LW and WN ADM scene type parameter intervals for clear, broken and overcast scenes.

Table 4 ΔT_s (°C) intervals corresponding to each percentile interval in Figure 15 for clear daytime and nighttime desert.

Table 5 ε intervals corresponding to each percentile interval considered in Figure 16 for broken cloud conditions over ocean and land.

Table 6 ε intervals corresponding to each percentile interval considered in Figure 17 for overcast conditions.

Figure 1

Sun

Satellite

θ_o

θ

ϕ

Figure 2

Figure 3

θ_{cld}

θ_{sfc}

h

I

cloud

III

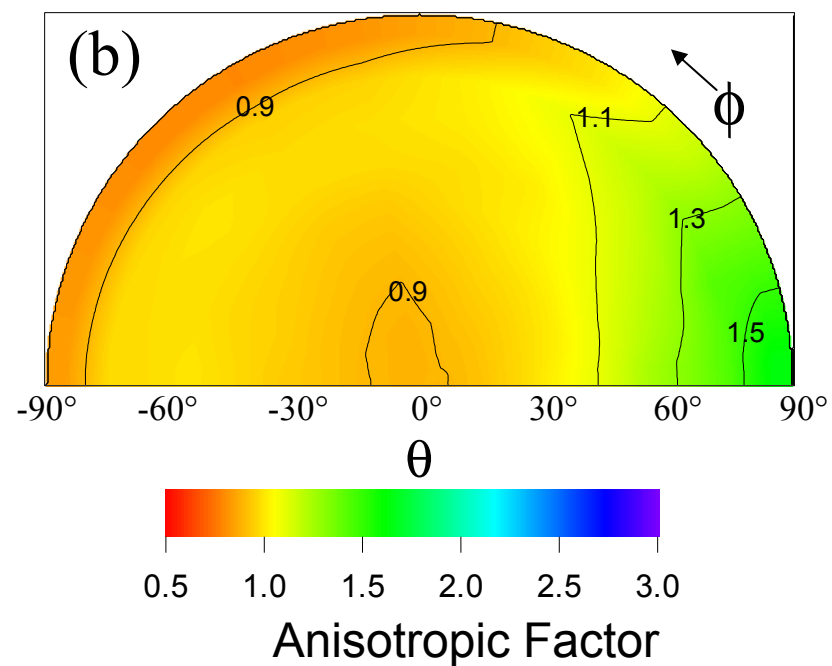II

Earth
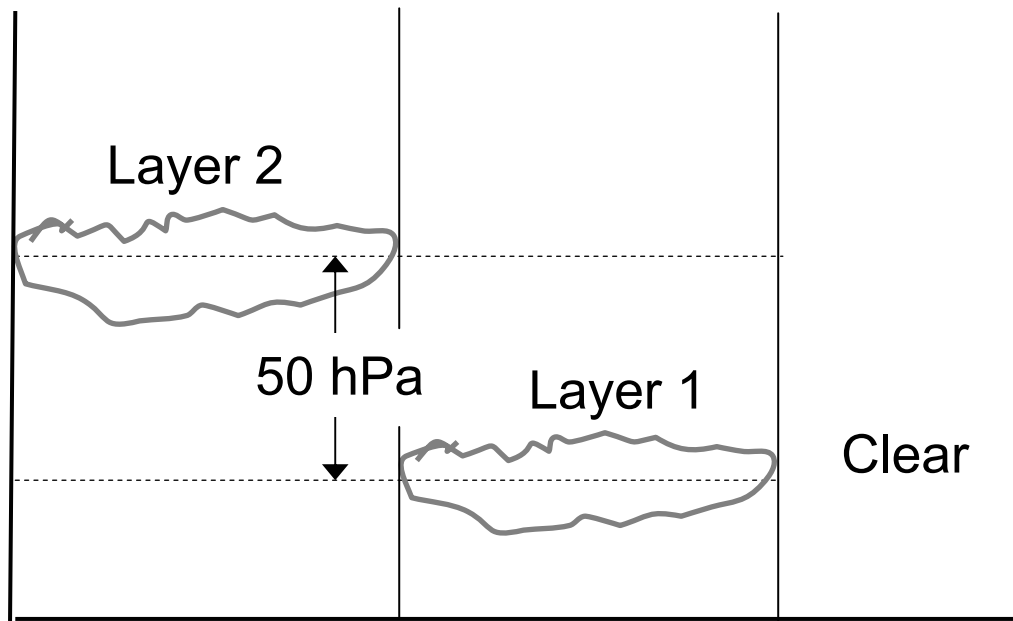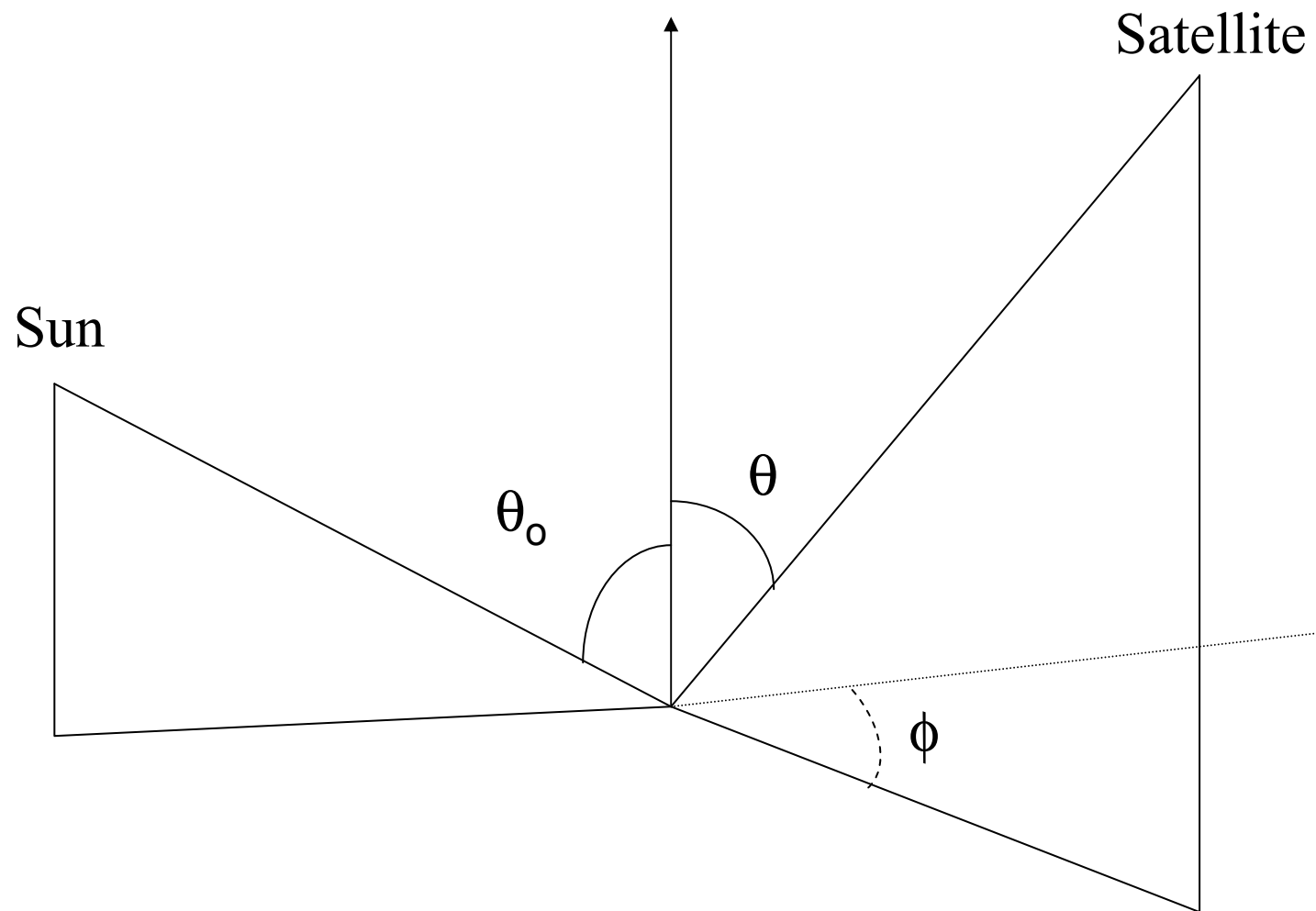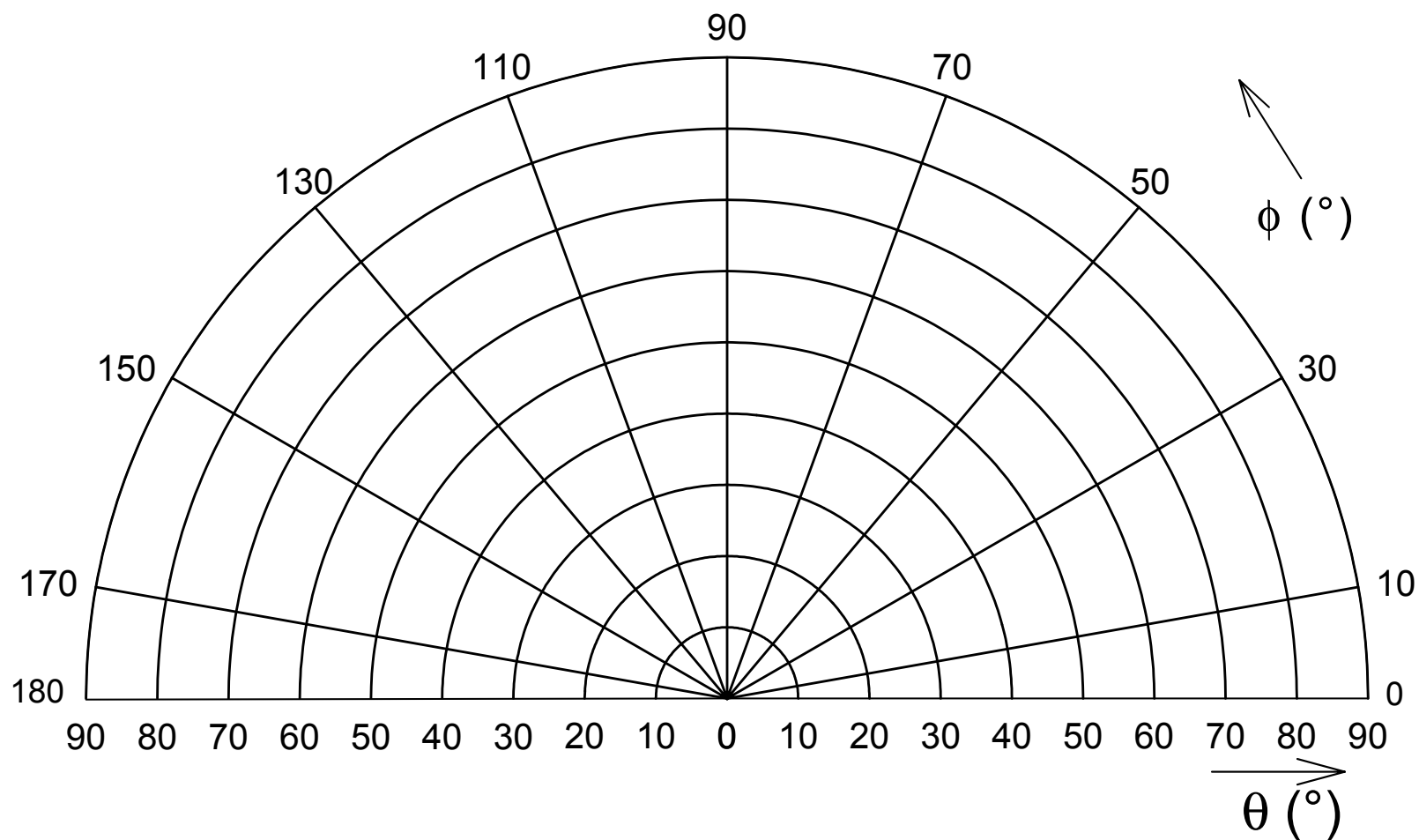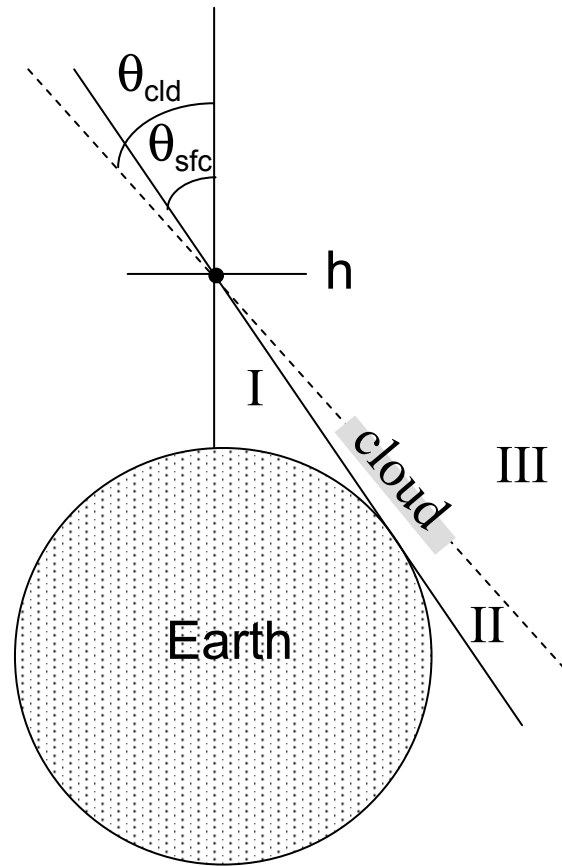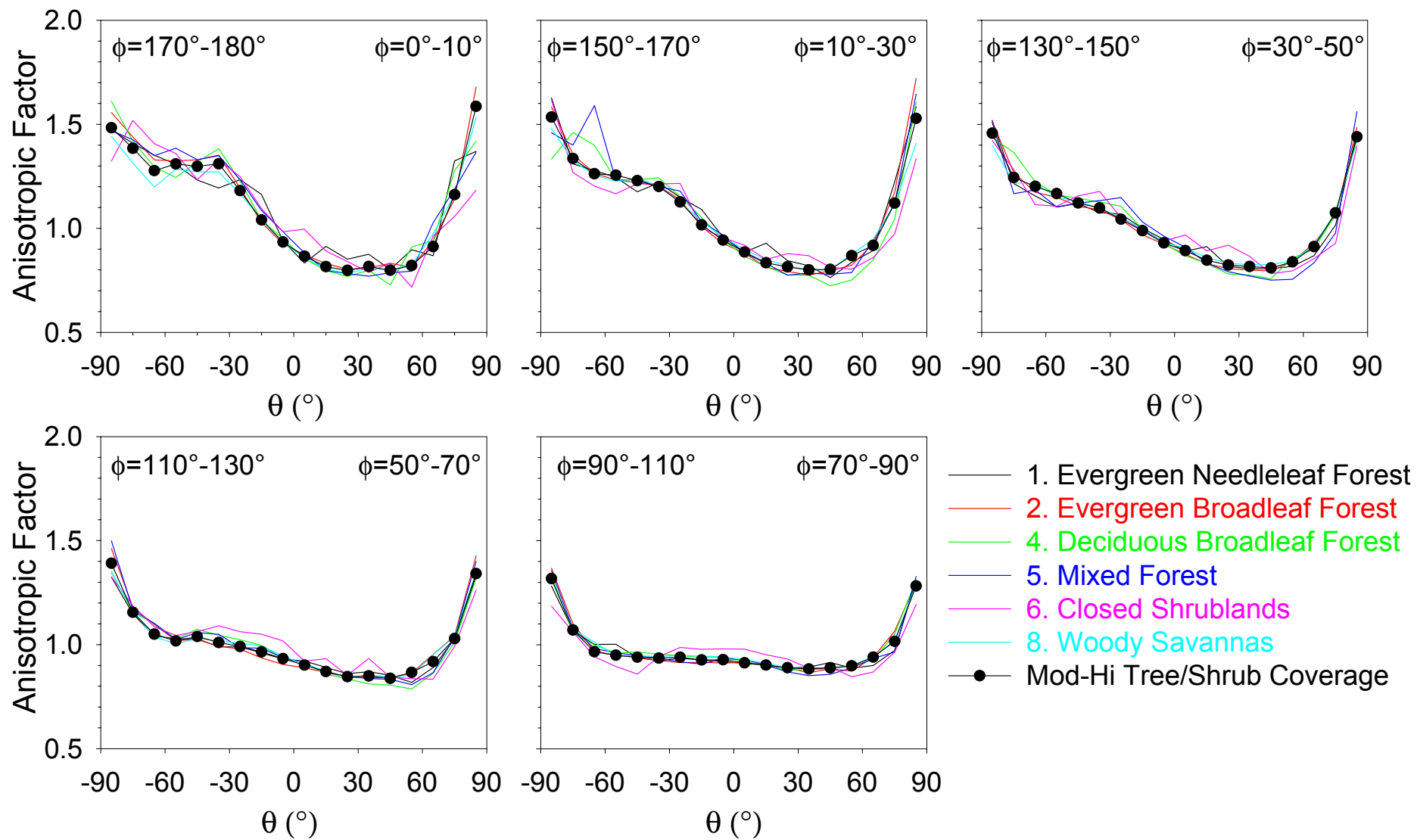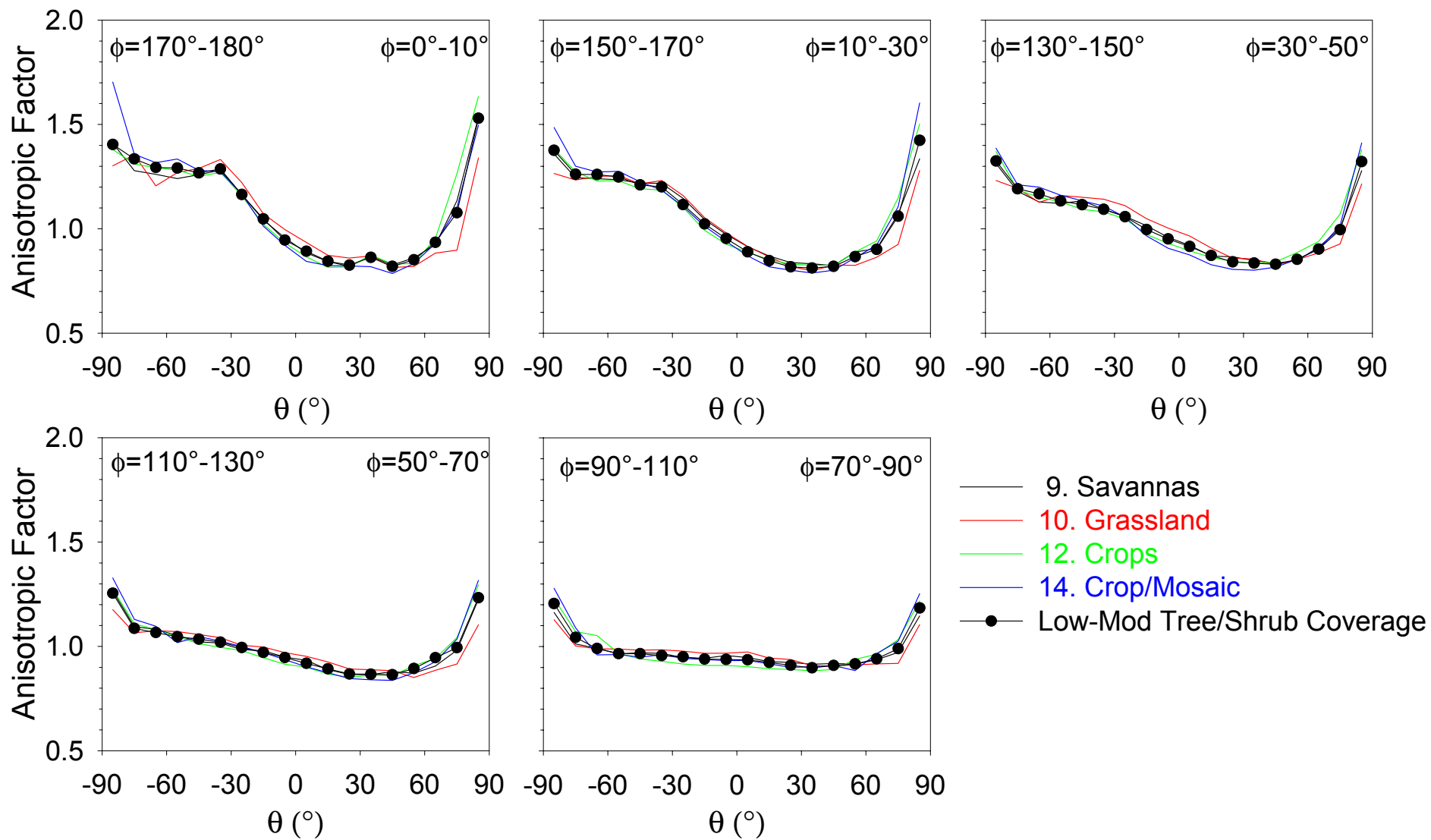
Figure 4
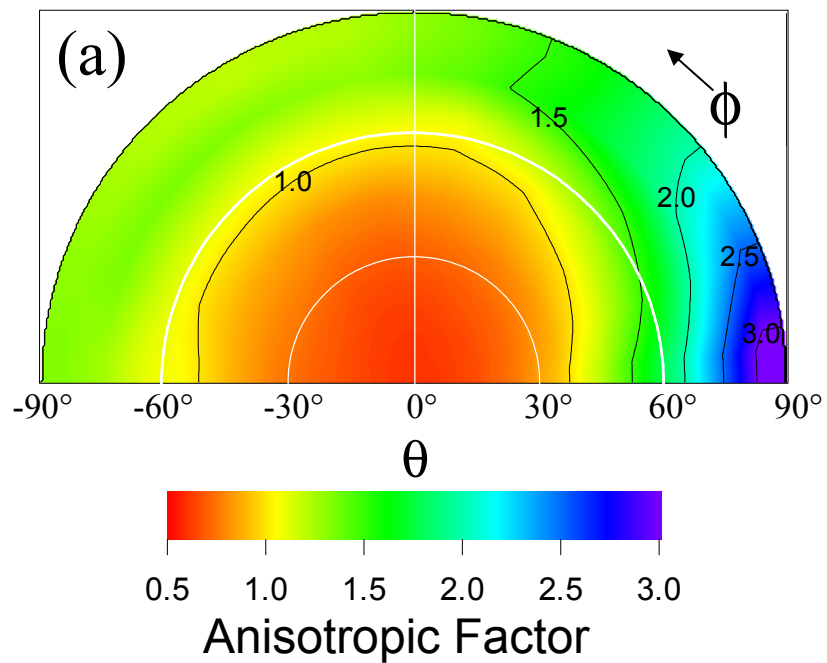
Figure 5
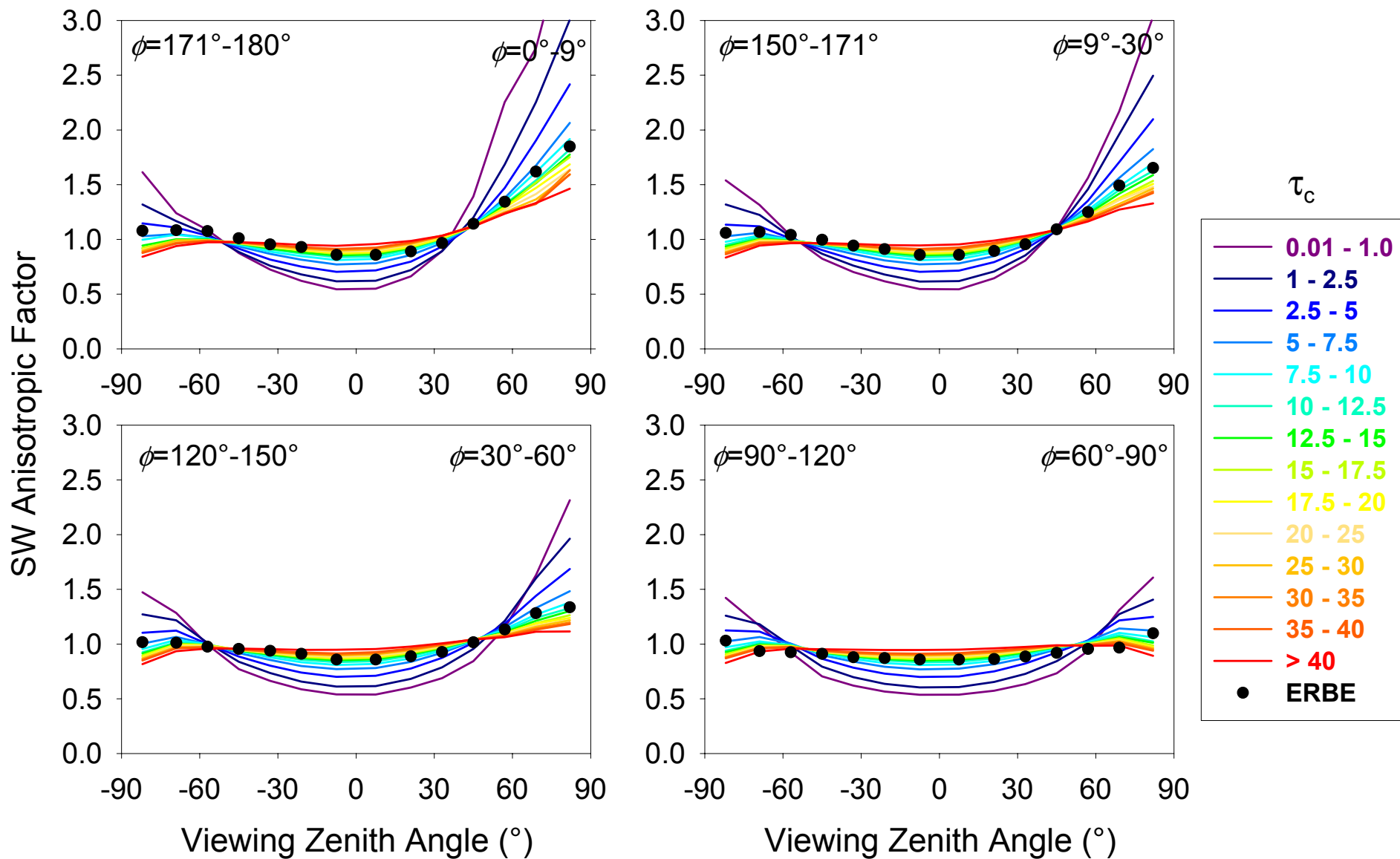
Figure 6
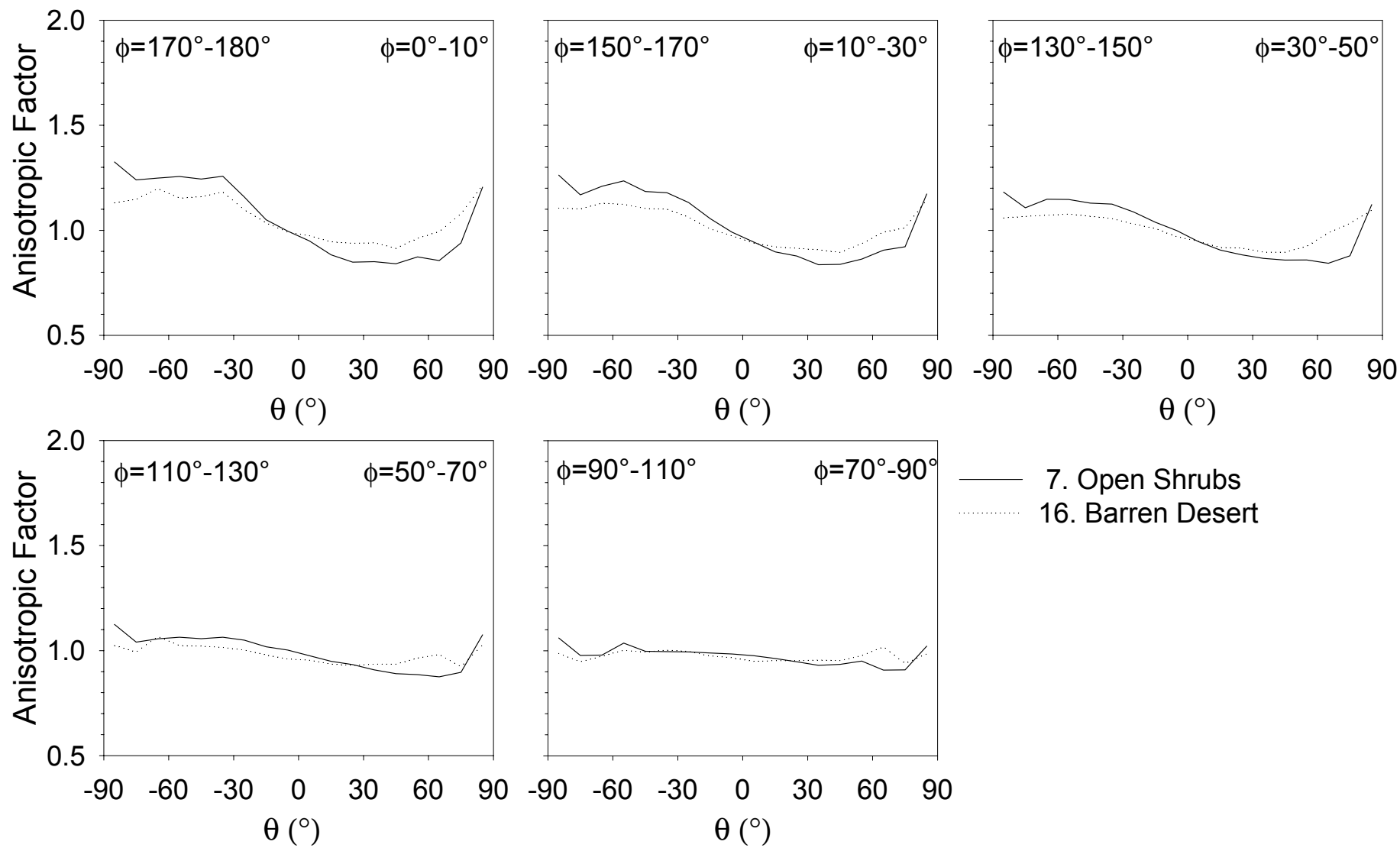
Figure 7
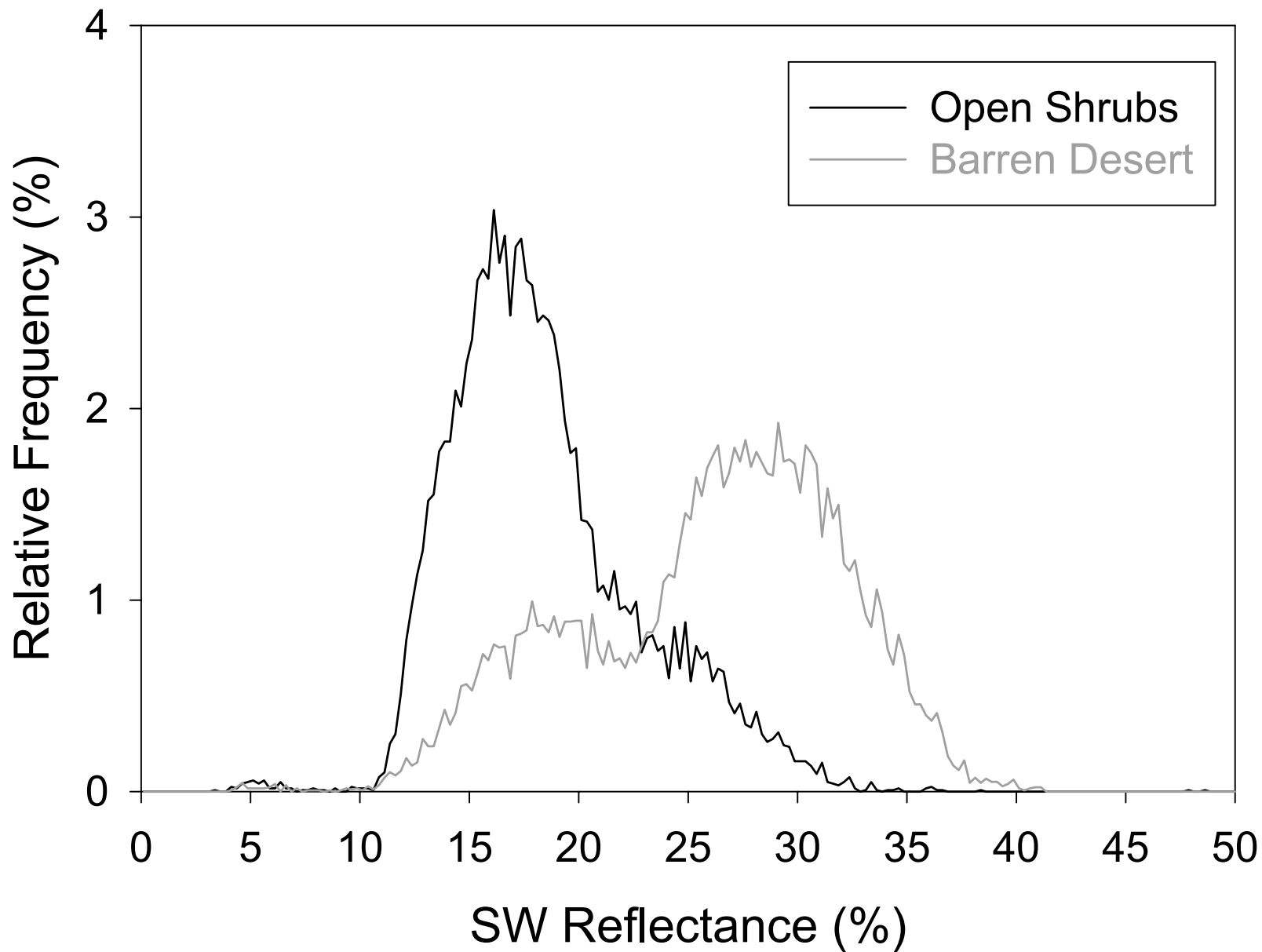
Figure 8
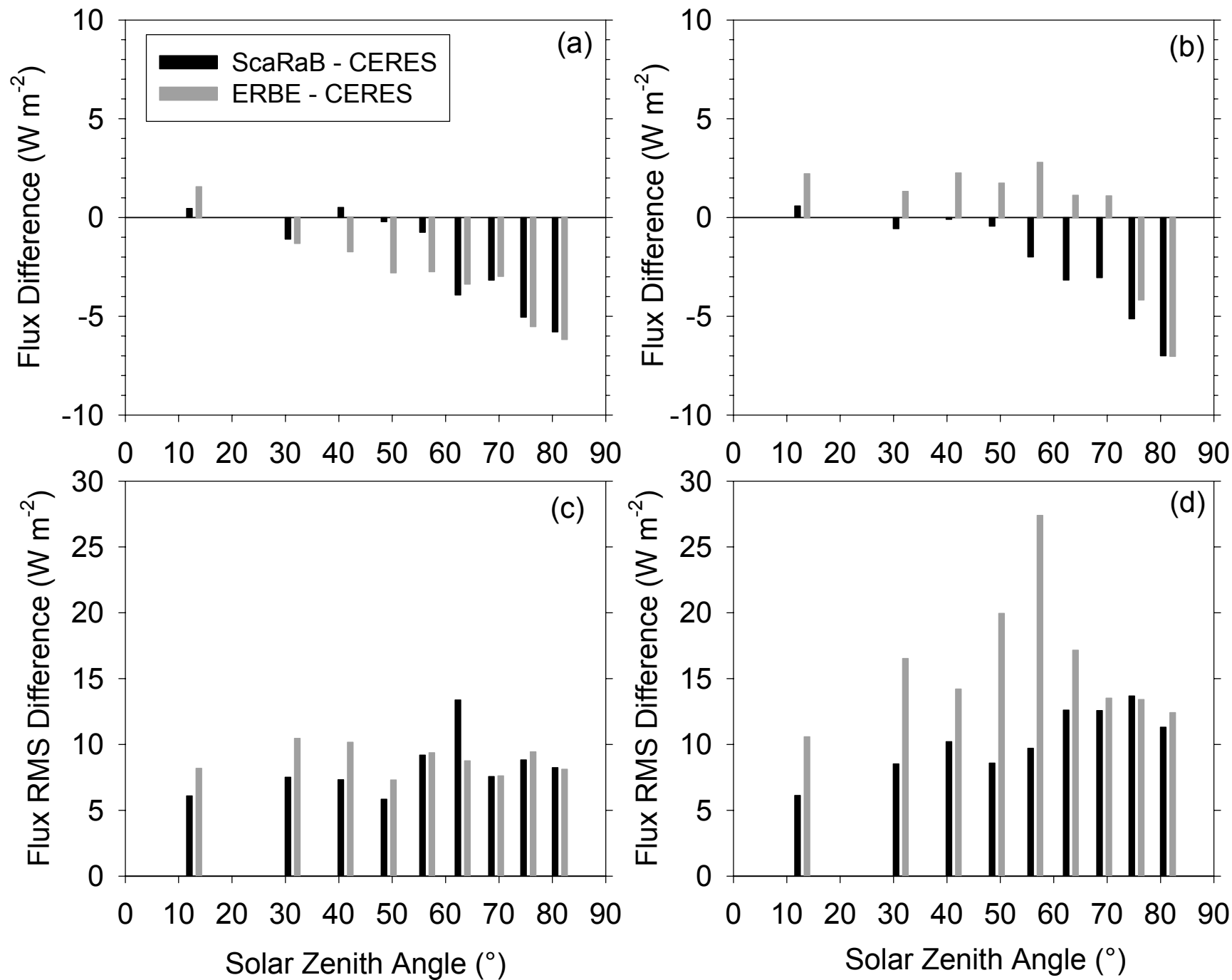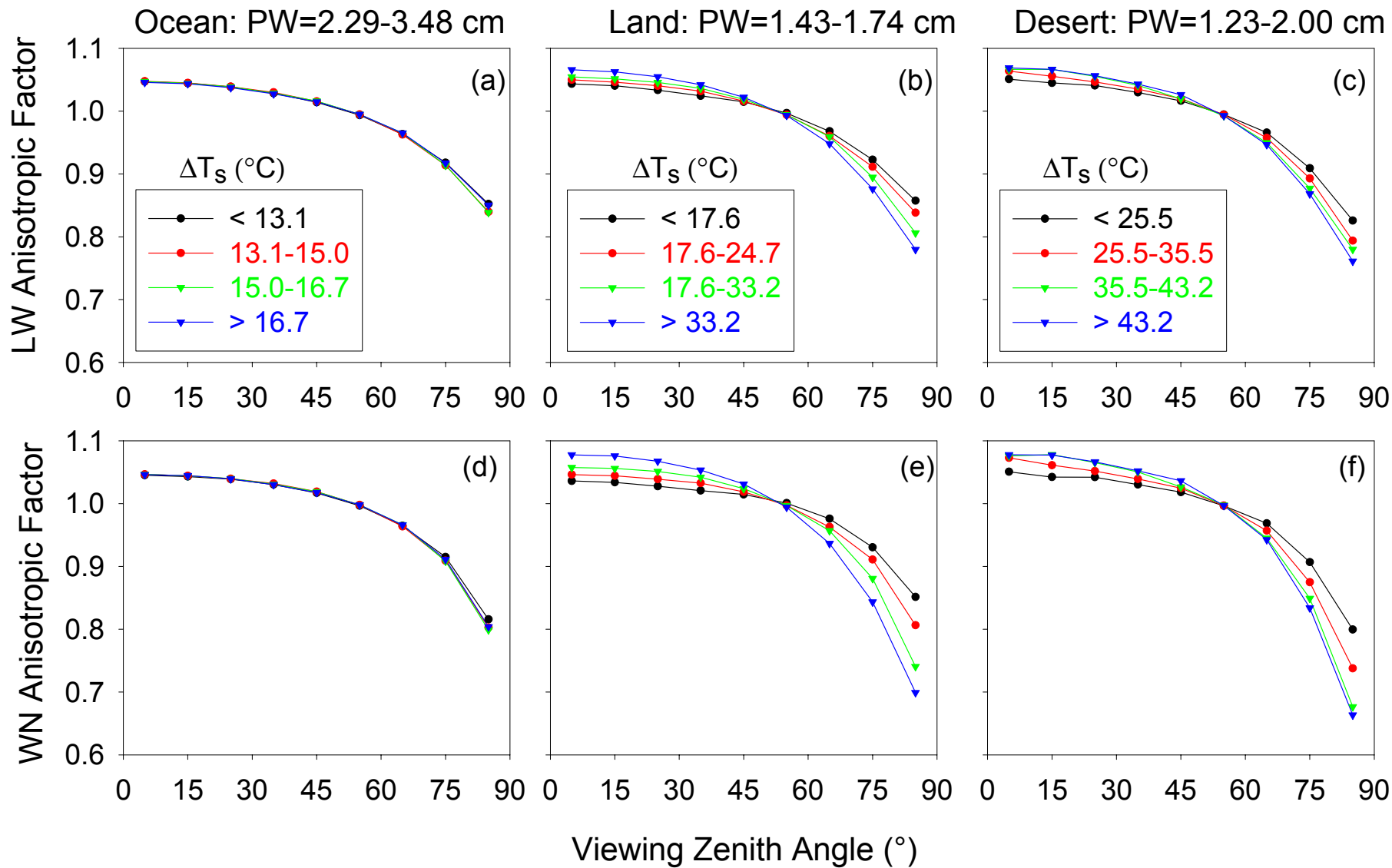
Figure 9
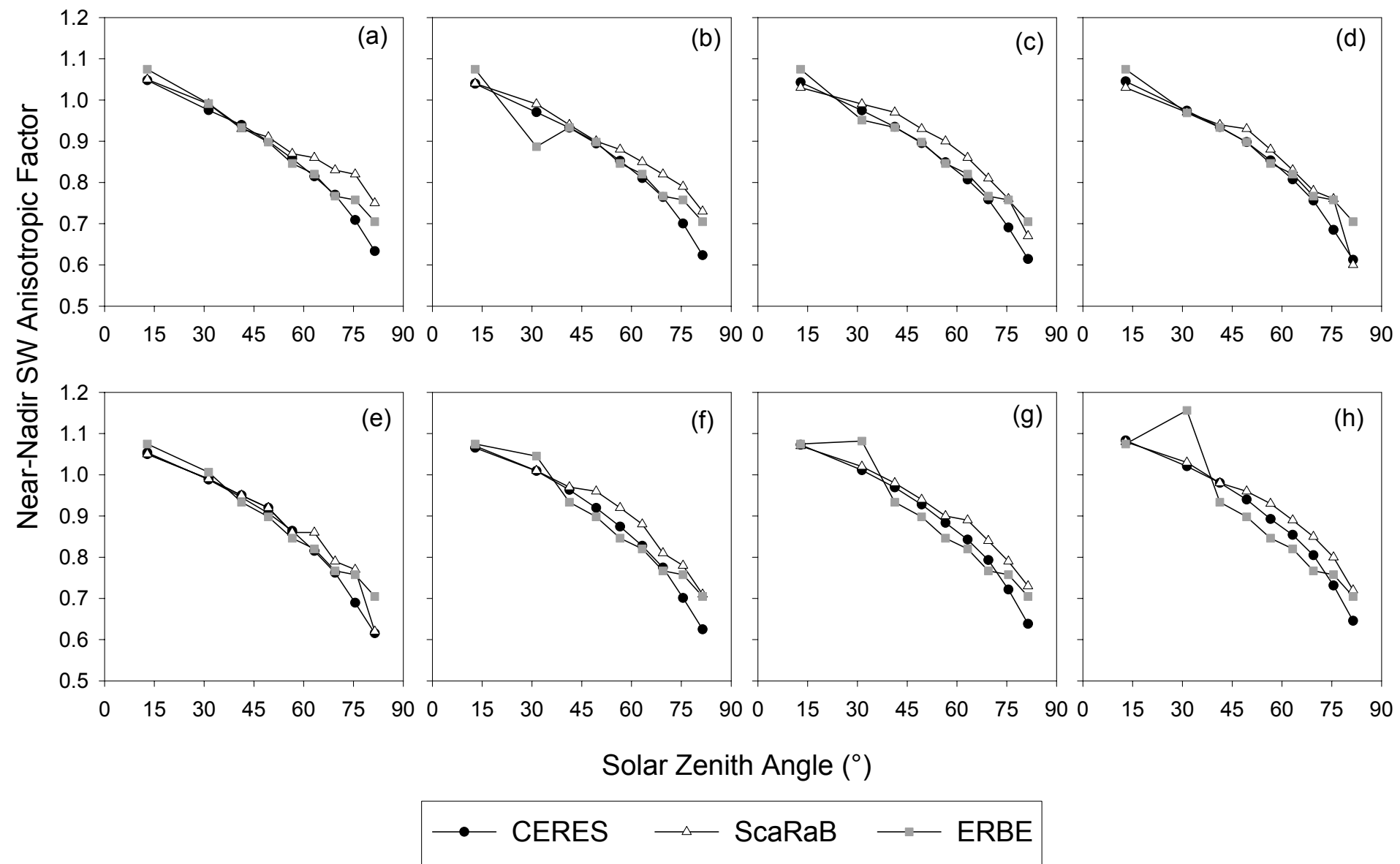
Figure 10
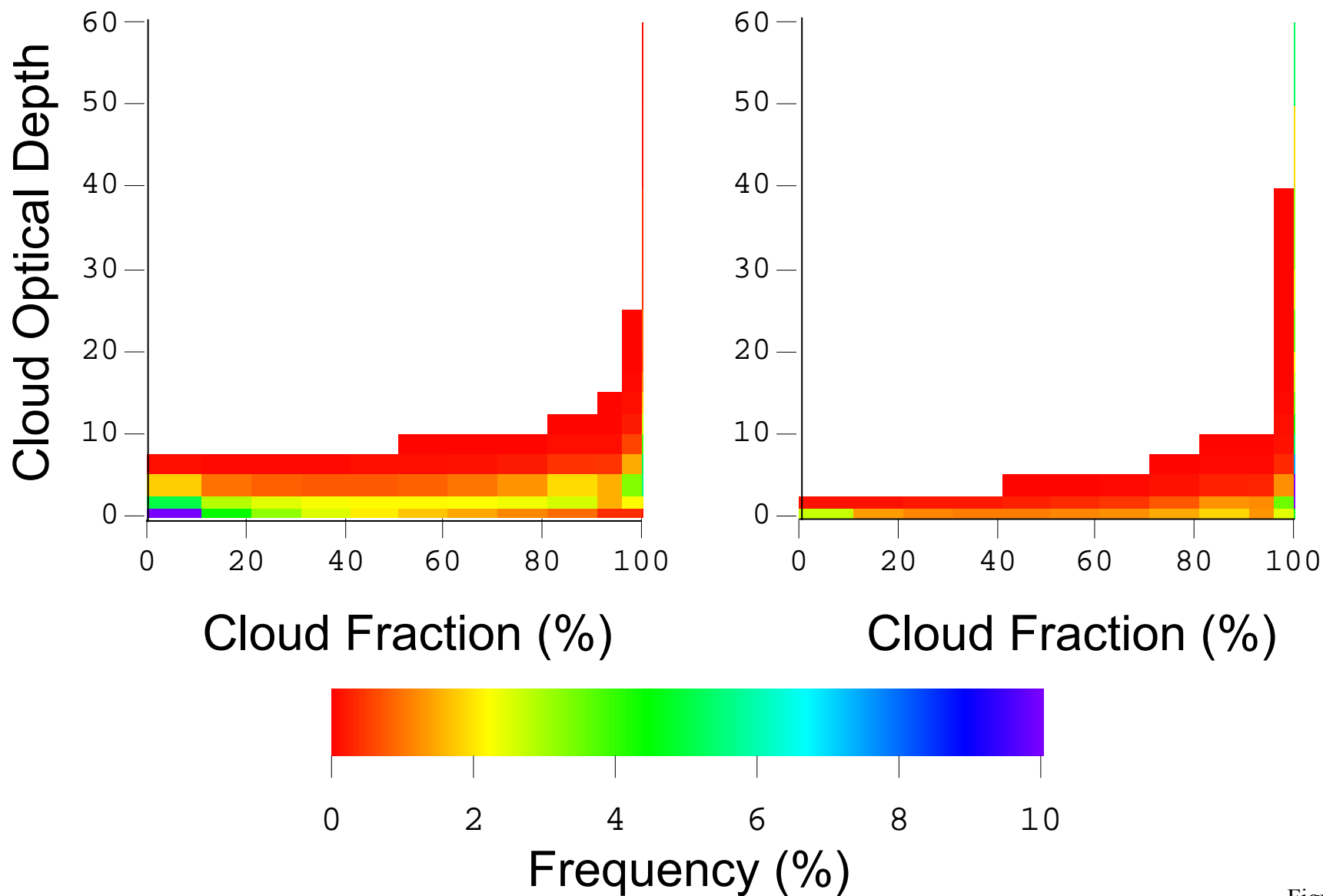
Figure 11
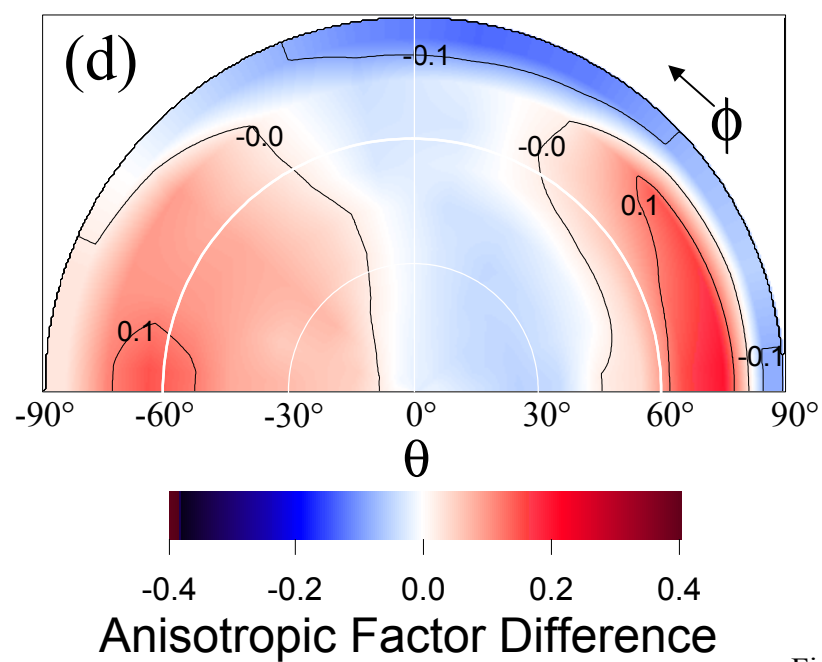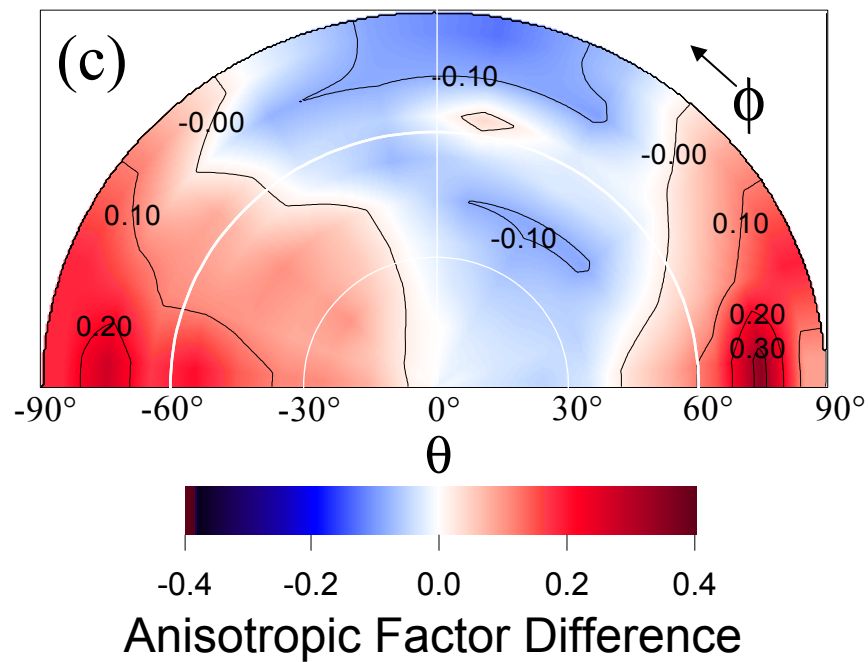
Figure 12

Figure 13

Figure 14
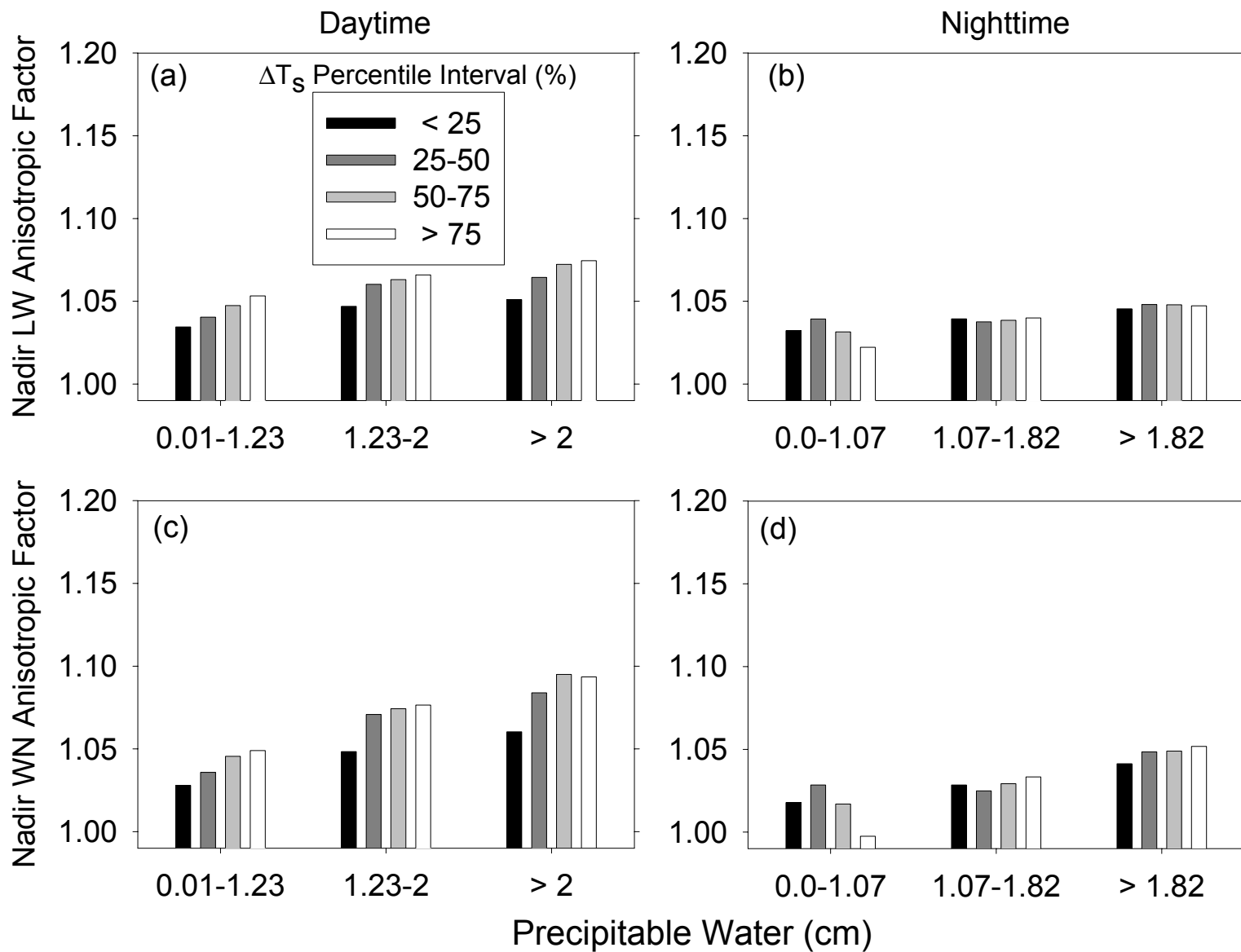
Figure 15
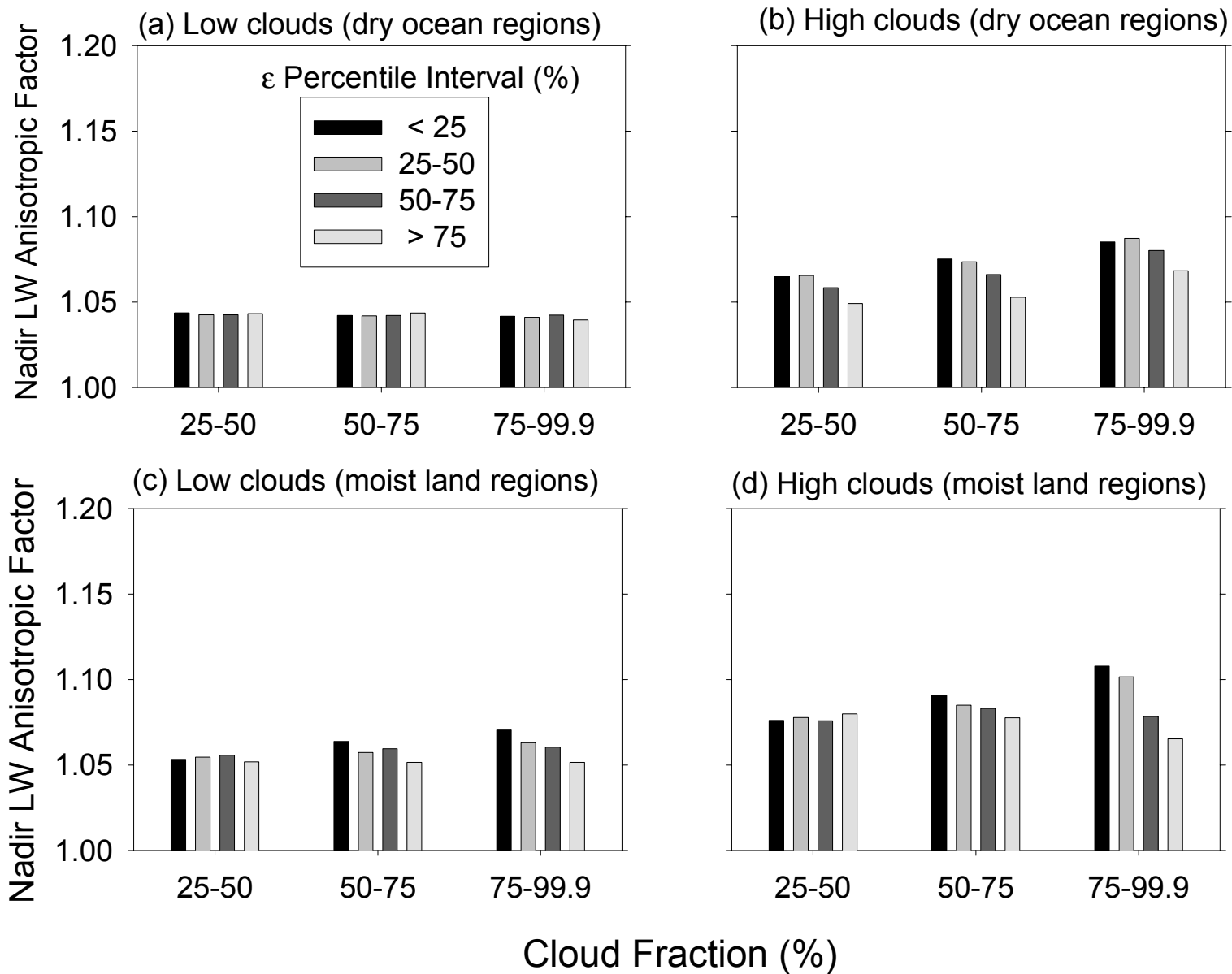
Figure 16
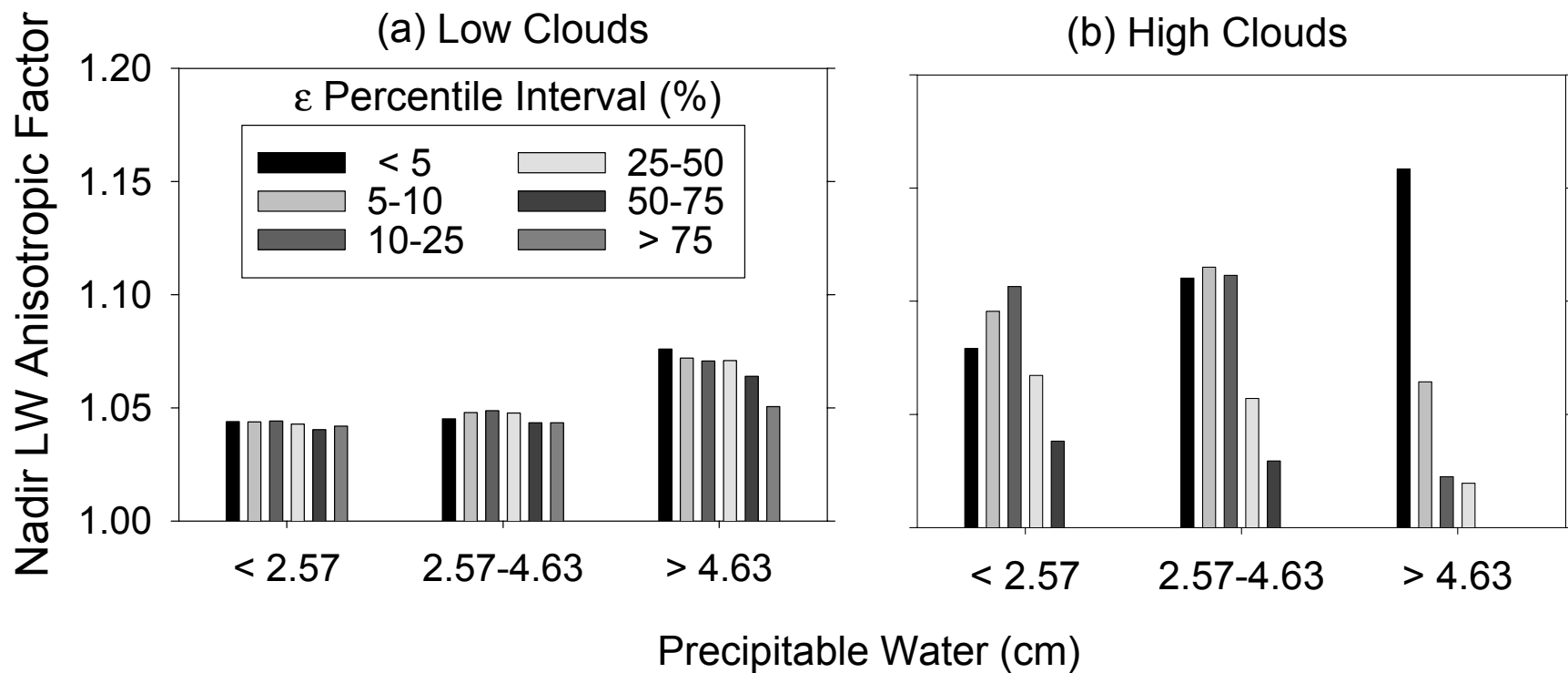
Figure 17

IGBP Type	Surface Type	Coverage (%)	Height (m)	Fraction (%)
1. Evergreen Needleleaf Forests	Trees	> 60	> 2	0.60
2. Evergreen Broadleaf Forests	Trees	>60	>2	1.71
3. Deciduous Needleleaf Forests	Trees	>60	>2	0.00
4. Deciduous Broadleaf Forests	Trees	>60	>2	0.55
5. Mixed Forests	Trees	>60	>2	0.43
6. Closed Shrublands	Woody Vegetation	>60	< 2	0.49
7. Open Shrubs	Woody Vegetation	10-60	< 2	10.14
8. Woody Savannahs	Herbaceous and other Understory systems	30-60	>2	2.73
9. Savannahs	Herbaceous and other Understory systems	10-30	>2	4.45
10.Grasslands	Herbaceous	< 10		3.97
11.Permanent Wetlands	Water and Herbaceous/Woody	> 60		0.02
12. Croplands	Temporary Crops followed by bare soil	-		4.32
13. Urban	Anthropogenic Structures (e.g. buildings, roads)	-		0.02
14. Cropland/ Natural Vegetation Mosaics	Mosaic of Croplands, Forests, Shrublands, and Grasslands	-		3.57
15. Snow and Ice	Snow and Ice			0.00
16. Barren Desert	Exposed soil, sand, rocks or snow	< 10		15.55
17. Water Bodies	Oceans, seas, lakes, reservoirs and rivers			50.22
18. Tundra	Tundra			0.01
19. Fresh Snow	Fresh Snow			1.21
20. Sea Ice	Sea Ice			0.00

Table 1 IGBP type classification scheme. "Coverage" refers to the fractional coverage of a surface type over 1×1 km^2 area; "Height" refers to the height of the vegetation; "Fraction" refers to the fraction of cloud-free CERES footprints in each IGBP type over the entire 9 months of daytime CERES/TRMM observations.

Surface Type	PSF-Weighted Phase Index	Cloud Fraction	Cloud Optical Depth
Ocean	< 1.5 (Liquid Water) > 1.5 (Ice)	0.1-10, 10-20, 20-30, 30-40, 40-50, 50-60, 60-70, 70-80, 80-90, 90-95,95-99.9, 99.9-100	0.01-1.0, 1.0-2.5, 2.5-5.0, 5.0-7.5, 7.5-10, 10-12.5, 12.5-15, 15-17.5, 17.5-20, 20-25, 25-30, 30-40, 40-50, >50
Mod-High Tree-Shrub Covg Low-Mod Tree-Shrub Covg Dark Desert Bright Desert	< 1.5 (Liquid Water) > 1.5 (Ice)	0.1-25, 25-50, 50-75, 75-99.9, 99.9-100	0.01-2.5, 2.5-6, 6-10, 10-18, 18-40, > 40

Table 2 SW ADM scene type parameter intervals for clouds over ocean, land and desert.

Cloud Category	Surface	Precipitable Water Percentile	Cloud Fraction (%)	Vertical Temperature Change Percentile	Cloud IR Emissivity Percentile	Total
Clear	Ocean Land Desert	≤ 33 33 - 66 ≥ 66	≤ 0.1	0-25 25 – 50 50 – 75 > 75 Inversion ($\Delta T_s < 0°C$)	-	45
Broken	Ocean Land Desert	≤ 33 33 - 66 ≥ 66	0.1 – 25 25 – 50 50 – 75 75 – 99.9	0 - 20 20 – 40 40 – 60 60 – 80 > 80 Inversion ($\Delta T_c < 0°C$)	0 - 25 25 - 50 50 – 75 > 75	288(O) 288(L) 288(D)
Overcast	All	≤ 33 33 - 66 ≥ 66	≥ 99.9	0 - 20 20 – 40 40 – 60 60 – 80 80 - 90 > 90 Inversion ($\Delta T_c < 0°C$)	0 – 5 5 – 10 10 – 25 25 – 50 50 – 75 > 75	126

Table 3 LW and WN ADM scene type parameter intervals for clear, broken and overcast scenes.

ΔT_s	Daytime			Nighttime		
Percentile	Precipitable Water Interval (cm)			Precipitable Water Interval (cm)		
Interval	< 1.23	1.23 – 2.0	> 2	< 1.07	1.07 – 1.82	> 1.82
< 25	0.0 – 18.0	0.0 – 25.5	0.0 – 28.7	0.0 – 5.8	0.0 – 10.0	0.0 -14.4
25 – 50	18.0 – 28.4	25.5 – 35.5	28.7 – 39.1	5.8 – 10.1	10.0 – 14.3	14.4 – 18.7
50 -75	28.4 – 38.9	35.5 – 43.2	39.1 – 46.6	10.1 – 14.9	14.3 – 18.9	18.7 – 22.5
> 75	> 38.9	> 43.2	> 46.6	> 14.9	> 18.9	> 22.5

Table 4 ΔT_s (°C) intervals corresponding to each percentile interval in Figure 14 for clear daytime and nighttime desert.

ε	Low Clouds (Dry Ocean Regions)			High Clouds (Dry Ocean Regions)		
Percentile Interval	f=25 – 50% ΔT_c=0.0 – 5.8 °C	f=50 – 75 ΔT_c=0.0 – 6.6 °C	f=75 – 99.9 ΔT_c=0.0 – 8.4 °C	f=25 – 50 $\Delta T_c > 14$°C	f=50 – 75 $\Delta T_c > 14.9$°C	f=75 – 99.9 $\Delta T_c > 19.2$ °C
< 25	< 0.389	< 0.454	< 0.595	< 0.281	< 0.351	< 0.436
25 – 50	0.389 – 0.513	0.454 – 0.581	0.595 – 0.733	0.281 – 0.403	0.351 – 0.501	0.436 – 0.614
50 -75	0.513 – 0.650	0.581 – 0.716	0.733 – 0.859	0.403 – 0.550	0.501 – 0.657	0.614 – 0.788
> 75	> 0.650	> 0.716	> 0.859	> 0.550	> 0.657	> 0.788
ε	Low Clouds (Moist Land Regions)			High Clouds (Moist Land Regions)		
Percentile Interval	f=25 – 50 ΔT_c=0.0 – 7.8 °C	f=50 – 75 ΔT_c=0.0 – 8.7 °C	f=75 – 99.9 ΔT_c=0.0 – 13.1 °C	f=25 – 50 $\Delta T_c > 32.8$ °C	f=50 – 75 $\Delta T_c > 34.6$ °C	f=75 – 99.9 $\Delta T_c > 44.2$ °C
< 25	< 0.584	< 0.653	< 0.793	< 0.239	< 0.308	< 0.457
25 – 50	0.584 – 0.709	0.653 – 0.765	0.793 – 0.885	0.239 – 0.358	0.308 – 0.449	0.457 – 0.691
50 -75	0.709 – 0.814	0.765 – 0.856	0.885 – 0.954	0.358 – 0.508	0.449 – 0.628	0.691 – 0.894
> 75	> 0.814	> 0.856	> 0.954	> 0.508	> 0.628	> 0.894

Table 5 ε intervals corresponding to each percentile interval considered in Figure 15 for broken cloud conditions over ocean and land.

ε	Low Clouds			High Clouds		
Percentile	$PW < 2.57$	$PW = 2.57 - 4.63$	$PW > 4.63$	$PW < 2.57$	$PW = 2.57 - 4.63$	$PW > 4.63$
Interval	$\Delta T_c = 0 - 11.8\ °C$	$\Delta T_c = 0 - 13.9\ °C$	$\Delta T_c = 0 - 32.8\ °C$	$\Delta T_c > 53.1\ °C$	$\Delta T_c > 64.9\ °C$	$\Delta T_c > 82.5\ °C$
$0 - 5$	< 0.704	< 0.582	< 0.509	< 0.347	< 0.359	< 0.782
$5 - 10$	$0.704 - 0.798$	$0.582 - 0.697$	$0.509 - 0.619$	$0.347 - 0.501$	$0.359 - 0.547$	$0.782 - 0.98$
$10 - 25$	$0.798 - 0.916$	$0.697 - 0.873$	$0.619 - 0.809$	$0.501 - 0.850$	$0.547 - 0.911$	$0.980 - 0.999$
$25 - 50$	$0.916 - 0.987$	$0.873 - 0.974$	$0.809 - 0.944$	$0.850 - 0.986$	$0.911 - 0.998$	$0.999 - 1.003$
$50 - 75$	$0.987 - 1.013$	$0.974 - 1.011$	$0.944 - 0.998$	$0.986 - 1.002$	$0.998 - 1.004$	-
> 75	> 1.013	> 1.011	> 0.998	-	-	-

Table 6 ε intervals corresponding to each percentile interval considered in Figure 16 for overcast conditions.

Cloud/Surface	Surface Properties	Aerosol or Cloud Properties
Clear Ocean	Ocean surface (Vermote et al., 1997) w_s=1.0, 2.5, 5.0, 7.5, 10 m s^{-1}	Maritime Tropical (Hess et al., 1998) (24 aerosol optical depths from 0.01 to 1.0)
Clear Land and Desert	Forest, Grass, Savannah, Alkali Flat, Bare Field, Prairie, Desert (Kriebel, 1977; Ahmad and Deering, 1992)	Continental Average, Desert (Hess et al., 1998) (24 aerosol optical depths from 0.01 to 1.0)
Cloud over Ocean	Ocean surface (Vermote et al., 1997) w_s=5.0 m s^{-1}	Stratus (Hess et al., 1998) (24 cloud optical depths from 0.1 to 200)
Cloud over Land and Desert	Forest, Grass, Prairie, Desert (Kriebel, 1977; Ahmad and Deering, 1992)	Cold Cirrus (Baum et al., 2000) (24 cloud optical depths from 0.1 to 200)

Table A.1 SW theoretical radiance database properties. w_s= wind speed.